Outflow Angles, Bulk Lorentz Factors, and Kinematics of Outflows from the Cores of AGN

Erick J. Guerra and Ruth A. Daly[1]
Department of Physics, Joseph Henry Laboratories,
Princeton University, Princeton, NJ 08544

ABSTRACT

Outflow angles and bulk Lorentz factors for 43 sources that have proper motions compiled by Vermeulen & Cohen (1994) are computed on the basis of Doppler factors and observed apparent motions in the plane of the sky. These estimates of outflow angles and bulk Lorentz factors are discussed along with their agreement with orientation unified models of AGN.

Intrinsic (i.e. rest frame) brightness temperatures computed by using the inverse Compton and equipartition Doppler factors are discussed along with their relevance to the "Inverse Compton catastrophe". Intrinsic luminosity densities and luminosities are presented, and the role of systematic errors is discussed.

These studies are carried out using a sample of 100 compact radio sources compiled by Ghisellini et al. (1993). Error estimates for previously computed inverse Compton Doppler factors and equipartition Doppler factors are presented for these sources, along with a few updates of these Doppler factor estimates.

Subject headings: BL Lacertae objects: general — galaxies: active — galaxies: kinematics and dynamics — quasars: general — radiation mechanisms: nonthermal — relativity

1. INTRODUCTION

It is generally accepted that relativistic outflows from the core regions of radio-loud active galactic nuclei (AGN) are responsible for many of the interesting phenomena that are observed in these sources. Relativistic motion of synchrotron emitting plasma will result in the Doppler boosting of the synchrotron radiation from these outflows (discussed by many authors, e.g. Marscher 1987). In addition, relativistic outflows would readily explain the apparent superluminal motion observed on VLBI (Very Long Baseline Interferometry) scales (e.g. Pearson & Zensus 1987).

[1]National Young Investigator

The Doppler factor is a key quantity in deriving intrinsic properties of an AGN. It is well known that the unbeamed flux density of a radiating source is related to the observed flux density by the Doppler factor. When combined with the apparent motion in the plane of the sky, the Doppler factor can be used to estimate the Lorentz factor and the viewing angle of an outflow, assuming the motion responsible for the Doppler boosting has the same speed as the motion of radio features in the plane of the sky (Ghisellini et al. 1993; Daly, Guerra, & Güijosa 1997). The values of these Lorentz factors and viewing angles are significant in understanding AGN physics and are relevant to orientation unified models of AGN.

There are several methods for computing the Doppler factor. One method, called the inverse Compton Doppler factor, is derived by assuming the observed X-ray flux is caused by inverse Compton scattering of synchrotron photons off the radiating particles (e.g. Marscher 1987). A second method, called the equipartition Doppler factor, is derived assuming that the sources are at or near equipartition of energy between radiating particles and magnetic field (Readhead 1994). Other methods (not discussed further here) include those based on variability measurements (Rees 1967) or jet/counter jet flux ratios (Conway 1982). Ghisellini et al. (1993; hereafter GPCM93) compute the inverse Compton Doppler factor for a sample of 105 sources, using data compiled from the literature. The data compiled by GPCM93 were used by Güijosa & Daly (1996) to compute equipartition Doppler factors. These sets of inverse Compton Doppler factors and equipartition Doppler factors are used here to compute the Lorentz factors, viewing angles, and intrinsic properties of outflows from these sources.

Updated estimates of both inverse Compton and equipartition Doppler factors for a sample of 100 sources are discussed in §2.1; intrinsic brightness temperatures computed for both sets of Doppler factors are discussed in §2.1.1. The reliability of Doppler factors and the errors assigned to these estimates are discussed in §2.2 and §2.3 respectively. Estimates of the intrinsic luminosity density and intrinsic luminosity are examined in §2.4. The computations of the bulk Lorentz factor and the viewing angle are discussed in §3. A subsample of sources with estimates of Doppler factors and apparent motion in the plane of the sky is introduced in §4.1, and a set of solutions for the bulk Lorentz factor and viewing angle are computed in §4.2 for this subsample. In §4.3, these results are discussed in the context of orientation unified models. A general discussion follows in §5.

2. A SAMPLE OF DOPPLER FACTOR ESTIMATES

2.1. Previous and Updated Doppler Factor Estimates

GPCM93 assemble the relevant data to compute the inverse Compton Doppler factor for those AGN with VLBI core size data available in the literature circa 1986-92. The five BL Lacs without known redshifts are excluded from the sample examined here, since inverse Compton and equipartition Doppler factor estimates depend on redshift (see eqs. A1 & A2). This leaves 100

sources in this sample which fall into the following classifications (GPCM93): 32 BL Lacerate objects (BL Lac), 53 core-dominated quasars (CDQ), 11 lobe-dominated quasars (LDQ), and 9 radio galaxies (RG). The CDQs are further classified on the basis of their optical polarization into 24 core-dominated high-polarization quasars (CDHPQ), 22 core-dominated low-polarization quasars (CDLPQ), and 7 core-dominated quasars without polarization information (CDQ-NPI). A detailed discussion of these classifications can be found in GPCM93.

Both the inverse Compton Doppler factor, δ_{IC}, and the equipartition Doppler factor, δ_{eq}, can be computed using the data compiled by GPCM93 (see the Appendix for the relevant formulae). By assuming that the observed radio frequencies and radio flux densities are the true peak radio frequencies and radio flux densities, GPCM93 use the data to compute δ_{IC}. This approximation is made since the multi-frequency observations and analysis of the radio spectra necessary to obtain true peak frequencies and flux densities are available for only a small fraction of these sources (e.g. Marscher & Broderick 1985, Unwin et al. 1994). Güijosa & Daly (1996) recompute δ_{IC} taking into account corrections to the angular size and flux density neglected by GPCM93 (see Appendix), and compute δ_{eq} with the same assumptions for this sample.

Both δ_{eq} and δ_{IC} are recomputed in this study assuming a deceleration parameter of $q_o = 0.05$ (i.e. $\Omega_o = 0.1$, $\Omega_\Lambda = 0$) and $h = 0.75$, and using updated VLBI data for four sources (1101+384, 0615+820, 1039+811, & 1150+812) from Xu et al. (1995); here Ω_o is the mean mass density relative to the critical value, Ω_Λ is the normalized cosmological constant, and Hubble's constant is parameterized in the usual way: $H_o = 100\ h$ km s^{-1} kpc^{-1}. When computing δ_{eq} and δ_{IC} for each source, we assume an optically thin spectral index $\alpha = 0.75$ ($S_\nu \propto \nu^{-\alpha}$) and a spherical geometry, as was done by GPCM93 and Güijosa & Daly (1996) (see eqs. A1 & A2). Note that δ_{eq} is changed by only a few percent relative to the values computed assuming an Einstein de-Sitter universe ($\Omega_o = 1.0$, $\Omega_\Lambda = 0$) and $h = 1$, while δ_{IC} is independent of these assumptions. Following GPCM93, upper bounds on angular sizes and lower bounds on redshifts are taken as detections in this section, but are treated as bounds when computing bulk Lorentz factors and viewing angles in §4.2.

Figures 1a & 1b show δ_{eq} and δ_{IC} respectively, computed as described in the Appendix, as functions of $(1+z)$. In these figures and throughout, solid circles represent BL Lacs, solid diamonds represent CDHPQs, solid squares represent CDLPQs, solid triangles represent CDQ-NPIs, open diamonds represent LDQs, and open squares represent RGs. The error estimates for δ_{eq} and δ_{IC} are discussed in §2.3. The trend in redshift is easily understood in terms of the effect of Doppler boosting on the observed flux density and the flux limited nature of this sample. Only at low redshift are we able to observe those sources with lower Doppler factors, and the sample is dominated by higher Doppler factors at all redshifts. It is also apparent that most LDQs and RGs have Doppler factors less than 1, and most CDQs have Doppler factors greater than one. BL Lacs have a much wider range of Doppler factors, covering the entire range of the whole sample.

Figure 2 shows the distribution of the equipartition Doppler factors, δ_{eq} (dotted line), and

the inverse Compton Doppler factors, δ_{IC} (dashed line), for all 100 sources in the sample; the horizontal axis is expressed in terms of $\log \delta$. Note that the distributions of δ_{eq} and δ_{IC} are similar, and both have a range of a few orders of magnitude. In addition, the peaks of both distributions are between 5 and 10. Figures 3a-f show the distribution of δ_{eq} (dotted line) and δ_{IC} (dashed line) for each class of AGN described above. For BL Lacs, the distributions range over a few orders of magnitude in δ, with a peak around $\delta \simeq 5$ (Figure 3a). CDHPQs have δ_{eq} and δ_{IC} that cover a smaller range of values than BL Lacs, and peak noticeably at about $\delta \simeq 10$ (Figure 3b), while the distribution of δ_{eq} and δ_{IC} for CDLPQs have a similar range as CDHPQs, and peak somewhere around $\delta \simeq 5$ (Figure 3c). CDQ-NPIs have the same range of δ_{eq} and δ_{IC} as CDHPQs and CDLPQs (Figure 3d). The distributions of δ_{eq} and δ_{IC} for LDQs are wider than those for RGs, but both classes peak at $\delta < 1$ (see Figures 3e & 3f).

The classification 3C216 as a LDQ should be examined closely since it has relatively large values for δ_{eq} and δ_{IC} (61 and 33 respectively). The separation of quasars into CDQ and LDQ was done by GPCM93 on the basis of the core dominance parameter computed using fluxes that were K-corrected to 5 Ghz. Recent observation by Reid et al. (1995) at 5 GHz give a core dominance parameter slightly greater than 1.0, and this would place 3C216 between the LDQs and CDQs in terms of the core dominance parameter. Most LDQs in this sample exhibit a triple morphology, consisting of a core with a flat radio spectrum and two lobes with steep radio spectra and have angular extents of about 10”-30” (e.g. Hooimeyer et al. 1992). 3C216 shows a triple morphology, but has an angular extent of only about 1.7”. It could be argued that 3C216 should be reassigned as a CDQ, but in this paper we keep this source in the LDQ sample but make a special note of it.

2.1.1. Brightness Temperatures

Both the equipartition Doppler factor and inverse Compton Doppler factor, δ_{eq} and δ_{IC}, are used here to compute the intrinsic peak brightness temperature for each source in the sample (see the Appendix for relevant formulae). Histograms of the observed brightness temperature, intrinsic brightness temperature base on δ_{eq}, and intrinsic brightness temperature base on δ_{IC} (T_{Bo}, $T_{Bi}(eq)$, and $T_{Bi}(IC)$) are shown in Figure 4 for all 100 sources, and in Figures 5a-f for each class of AGN. Table 1 lists the mean and the standard deviation of the mean of T_{Bo}, $T_{Bi}(eq)$, and $T_{Bi}(IC)$ for the full sample and each class.

The observed peak brightness temperatures span a few orders of magnitude even within some individual classes of AGN. In contrast, there is a sharp peak in the distribution of the estimates of intrinsic brightness temperature, $T_{Bi}(eq)$ and $T_{Bi}(IC)$, and both are centered around about 7.5×10^{10} K. These two estimates of the intrinsic brightness temperature agree well with each other, which is not surprising given the strong correlation between δ_{eq} and δ_{IC} described above and by Güijosa & Daly (1996).

It is interesting to note that the mean $T_{Bi}(IC)$ for all classes (except CDQ-NPIs) are

consistent within 1σ, while the LDQs and RGs have larger $T_{Bi}(eq)$ than the other classes at about the 2σ level. These two classes have values of $R = \delta_{eq}/\delta_{IC}$ less than one (Güijosa & Daly 1996), which could possibly be due to a systematic underestimate of δ_{eq} by about 75%. Such an underestimate of δ_{eq} could account for the larger $T_{Bi}(eq)$ found for LDQs and RGs.

The standard deviations of $T_{Bi}(eq)$ and $T_{Bi}(IC)$ are 0.27×10^{11} K and 0.33×10^{11} K respectively. It should be noted that $T_{Bi}(eq) \propto S_{op}^{0.1}\nu_{op}^{0.3}\theta_d^{0.3}$ and $T_{Bi}(IC) \propto S_{op}^{0}\nu_{op}^{-0.7}\theta_d^{-0.4}$ which are weak dependences on observable, much weaker than the dependences of T_{Bo} on the same parameters. If the range of values for the observables that go into $T_{Bi}(eq)$ and $T_{Bi}(IC)$ are not too large, then their narrow distributions can be explained by weak dependences on observable parameters. The range of θ_d contributes the most to the range of $T_{Bi}(eq)$ and $T_{Bi}(IC)$, since ν_{op} is fixed at discrete values corresponding to the frequencies of observations, and S_{op} is virtually insignificant in computing $T_{Bi}(eq)$ and $T_{Bi}(IC)$. If the narrow ranges of $T_{Bi}(eq)$ and $T_{Bi}(IC)$ are due to some physical cause and not the range in θ_d, then randomly reassigning the angular sizes used to compute $T_{Bi}(eq)$ and $T_{Bi}(IC)$ should widen the distributions of each. When the angles are reassigned randomly, the means are quite similar (0.85×10^{11} K and 0.79×10^{11} K respectively), and the standard deviations are 0.26×10^{11} K and 0.43×10^{11} K respectively. Each width is not significantly affected by randomly reassigning angular sizes, which suggests that the narrow range of $T_{Bi}(eq)$ and $T_{Bi}(IC)$ obtained here is primarily due to the range of observables, and are probably not due to the physical state of the sources.

Readhead (1994) points out that if the intrinsic brightness temperatures were cutoff due to the inverse Compton catastrophe (i.e. the radiation lifetime plays a role in the observed cutoff), one would expect the intrinsic brightness temperatures of compact radio sources to cluster near $10^{11.5}$ K. Both estimates of intrinsic brightness temperatures for this sample peak below $10^{11.5}$ K which agrees with the results of Readhead (1994). This suggests that the inverse Compton catastrophe does not play a role in the observed brightness temperature distribution, or if the peaks are set by the inverse Compton catastrophe, a factor of about 4 has not been accounted for in computing the unbeamed brightness temperatures.

2.2. Reliability of δ_{eq} and δ_{IC} as Estimators of the Doppler Factor

Previous results indicate that $\delta_{eq} \simeq \delta_{IC}$ for this sample (Güijosa & Daly 1996). To further test this conclusion, the effect of randomly reassigning one of the observable quantities used to compute δ_{eq} and δ_{IC} is examined. Since both Doppler factors depend strongly on angular size ($\delta_{eq} \propto \theta_d^{-2.3}$ and $\delta_{IC} \propto \theta_d^{-1.6}$), the angular sizes used to compute δ_{eq} and δ_{IC} were randomly reassigned between sources within each class, and the mean values are shown in Table 2. Note that the means of δ_{eq} and δ_{IC} tend to systematically increase from their true values for all classes when the angular sizes are reassigned.

The fractional uncertainties in the mean values of δ_{eq} and δ_{IC} are of order 20% to 30%, so

that the mean δ_{eq} and δ_{IC} are significant at about the 3σ to 5σ level (Güijosa & Daly 1996). In contrast, the "random" mean values are significant at 2σ or less (i.e. their uncertainties are greater than 50%, Table 2). This suggests that these Doppler factor estimate are reliable.

2.3. Errors for the Doppler Factor Estimates

The main source of error for both Doppler factor estimates is the assumption that the radio flux density and frequency used to compute the Doppler factor are the peak radio flux density and peak frequency. Thus, an estimate of errors for this data set should focus on systematic errors instead of statistical ones. A dependence of observed angular sizes on frequency occurs if the synchrotron-emitting plasma has gradients in magnetic field and particle density (Marscher 1977, 1987), but since the model considered here is that of a uniform sphere, the errors associated with this frequency dependence of angular size are neglected.

The computed errors are found by assuming all sources have the same fractional errors on the peak frequency, ν_{op}; this uncertainty is likely of order 100% and dominates all other sources of error, as discussed in Güijosa & Daly (1996). It is assumed that the flux density has an error which is related to the spectral index between the observed frequency and the peak frequency, α_{op}, where $S_{op} = S_o(\nu_{op}/\nu_o)^{-\alpha_{op}}$ and S_o and ν_o are the observed flux density and frequency; α_{op} should not to be confused with the optically thin spectral index, α. In terms of VLBI observed properties, $\delta_{eq} \propto S_{op}^{1.1}\nu_{op}^{-2.3}\theta_d^{-2.3}$ and $\delta_{IC} \propto S_{op}^{1.0}\nu_{op}^{-1.3}\theta_d^{-1.6}$, assuming $\alpha = 0.75$. These two Doppler factor estimates can be related to the ratio of the peak frequency to the observed frequency, $\delta_{eq} \propto (\nu_{op}/\nu_o)^{-1.1\alpha_{op}-2.3}$ and $\delta_{IC} \propto (\nu_{op}/\nu_o)^{-1.0\alpha_{op}-1.3}$. One finds that

$$\frac{\sigma\delta_{eq}}{\delta_{eq}} = (1.1\alpha_{op} + 2.3)\left(\frac{\sigma\nu_{op}}{\nu_{op}}\right) \qquad \text{and} \qquad \frac{\sigma\delta_{IC}}{\delta_{IC}} = (1.0\alpha_{op} + 1.3)\left(\frac{\sigma\nu_{op}}{\nu_{op}}\right), \tag{1}$$

where $\sigma\delta_{eq}$, $\sigma\delta_{IC}$, and $\sigma\nu_{op}$ are the error estimates for δ_{eq}, δ_{IC}, and ν_{op}.

An estimate of $\sigma\nu_{op}/\nu_{op}$ is needed to assign errors for the Doppler factor estimates using equation (1). A reasonable value of $\sigma\nu_{op}/\nu_{op}$ is that which gives a reduced χ^2 of 1.0 when fitting $R \equiv \delta_{eq}/\delta_{IC}$ to unity.

Since $R \propto S_{op}^{0.1}\nu_{op}^{-1.0}\theta_d^{-0.7}$ for $\alpha = 0.75$, it can be shown that $R \propto (\nu_{op}/\nu_o)^{-0.1\alpha_{op}-1.0}$. The error on the ratio R, denoted σR, can be related to $\sigma\nu_{op}/\nu_{op}$ by

$$\frac{\sigma R}{R} = (0.1\alpha_{op} + 1.0)\left(\frac{\sigma\nu_{op}}{\nu_{op}}\right). \tag{2}$$

Note that if $\sigma\nu_{op}/\nu_{op}$ and α_{op} are the same for all sources, then $\sigma R/R$ is the same for all sources.

The value of $\sigma R/R = 0.61$ gives a reduced χ^2 of 1.0 when fitting R to a constant equal to unity for all sources. A value of $\alpha_{op} = 0.4$ is assumed for all sources since radio sources with observed optically thin spectral indices for their cores have spectral indices in the range of about

0.5 to 1, and the spectral index must go to zero towards the peak. A lower value of α_{op} could be used, and this will decrease the errors slightly on δ_{eq} and δ_{IC}. For $\alpha_{op} = 0.4$ and $\sigma R/R = 0.61$, equation (2) gives $\sigma\nu_{op}/\nu_{op} = 0.59$, and one finds that $\sigma\delta_{eq}/\delta_{eq} = 1.6$ and $\sigma\delta_{IC}/\delta_{IC} = 1.0$ using equation (1). These error estimates for δ_{eq} and δ_{IC} are adopted throughout this paper.

Some objects in this sample have been observed at multiple frequencies, and spectra are available in the literature. The observed frequencies used to compute the Doppler factors for eight of the sources studied here are compared to the peak frequencies of the integrated spectra available in Xu et al. (1995), in order to check if our estimate of $\sigma\nu_{op}/\nu_{op}$ is reasonable. It should be noted that the integrated spectra include components besides the cores, and that the core component is used to determine the Doppler factor (see §5). Here we approximate that the peak of the integrated spectra corresponds to the peak of the core. On this basis, four sources have $\sigma\nu_{op}/\nu_{op}$ between 0 and 0.5, and the other four have $\sigma\nu_{op}/\nu_{op}$ between 0.5 and 4, which would indicate that the value of $\sigma\nu_{op}/\nu_{op} = 0.59$ adopted for the whole sample is quite reasonable.

2.4. Luminosity Densities and Luminosities

The uncorrected luminosity density is given by

$$L_{\nu_{un}} = 4\pi(a_o r)^2(1+z)S_o, \tag{3}$$

where S_o is the observed flux density, z is the source redshift, $(a_o r)$ is the coordinate distance to the source, and ν_{un} is frequency as would be measured in the local Hubble frame of the source without correcting for Doppler boosting ($\nu_{un} = \nu_o(1+z)$ where ν_o is the observed frequency). The flux density corrected for Doppler boosting of a uniform spherical source, S_i, is given by $S_i = S_o/\delta^3$, where δ is the Doppler factor. The corrected flux density is the flux density that would be received by an observer moving with the same velocity with respect to the Hubble flow as the radiating source. Substituting S_i for S_o in equation (3) gives the Doppler corrected, or intrinsic, luminosity density:

$$L_{\nu i} = 4\pi(a_o r)^2\frac{1+z}{\delta^3}S_o \tag{4}$$

where $\nu_i = \nu_o(1+z)/\delta$. Substituting both estimates of the Doppler factor δ_{eq} and δ_{IC} into equation (4) gives two sets of intrinsic luminosity densities which shall be referred to as $L_{\nu i}(eq)$ and $L_{\nu i}(IC)$ respectively.

It should be noted that equations (3) and (4) are the luminosity densities at frequencies that differ from the observing frequencies, which are $\nu_{un} = \nu_o(1+z)$ and $\nu_i = \nu_o(1+z)/\delta$ respectively. Thus, the uncorrected luminosity can be approximated as $L_{un} \approx L_{\nu_{un}}\nu_o(1+z)$, and the intrinsic luminosity can be approximated as

$$L_i \approx L_{\nu i}\nu_o(1+z)/\delta. \tag{5}$$

Note that luminosities computed in this manner are crude approximations that may be systematically biased by the approximated peak frequencies, yet still give order of magnitude estimates.

Figures 6 & 7 show $L_{\nu_{un}}$ and L_{un} as functions of $(1+z)$. The flux-limited nature of this sample is evident in these two figures, and it is quite obvious that selection effects play a role in the composition of this sample. The intrinsic luminosity densities, $L_{\nu i}(eq)$, are plotted versus the rest frame frequency $\nu_i(eq)$ in Figure 8, and $L_i(eq)$ versus $\nu_i(eq)$ is plotted in Figure 9. By fitting all the data plotted in Figures 8 and 9, one finds that $L_{\nu i}(eq) \propto \nu_i(eq)^{2.3\pm0.1}$ with a reduced χ^2 equal to 4.6 and a correlation coefficient $r = 0.91$, and $L_i(eq) \propto \nu_i(eq)^{3.3\pm0.1}$ with a reduced χ^2 equal to 4.0 and a correlation coefficient $r = 0.96$. Both of these power law fits are very significant since r is close to unity. Figures 10 and 11 show $L_{\nu i}(eq)$ and $L_i(eq)$ respectively as functions of $(1+z)$; fitting all these data, one finds that $L_{\nu i}(eq) \propto (1+z)^{2.5\pm1.6}$ with a reduced χ^2 equal to 1.3 and a correlation coefficient $r = 0.16$, and $L_i(eq) \propto (1+z)^{0.9\pm2.2}$ with a reduced χ^2 equal to 1.4 and a correlation coefficient $r = 0.04$. Similar results are found for $L_{\nu i}(IC)$ and $L_i(IC)$.

Figures 8 & 9 show a trend in $L_{\nu i}(eq)$ and $L_i(eq)$ with $\nu_i(eq)$ that can be explained by the strong dependence of these quantities on the Doppler factor and a systematic effect introduced by assuming the observed frequency is the peak frequency. Equations (4) & (A2) indicate that $L_{\nu i}(eq) \propto {\delta_{eq}}^{-3} \propto \nu_{op}^{6.9}$ and that $\nu_i(eq) \propto \nu_{op}{\delta_{eq}}^{-1} \propto \nu_{op}^{3.3}$, for $\alpha = 0.75$. Since it is assumed that $\nu_{op} = \nu_o$ when computing δ_{eq}, the offset of ν_o/ν_{op} from unity will cause $L_{\nu i}(eq)$ to be offset by a factor of $(\nu_o/\nu_{op})^{6.9}$ and $\nu_i(eq)$ to be offset by a factor of $(\nu_o/\nu_{op})^{3.3}$ from their actual values. One would expect to find a systematic effect that would increase the range of $L_{\nu i}(eq)$ and $\nu_i(eq)$ such that $L_{\nu i}(eq) \propto \nu_i(eq)^{2.1}$. In fact, one obtains $L_{\nu i}(eq) \propto \nu_i(eq)^{2.3\pm0.1}$ by fitting the data in Figure 8. A similar calculation gives the prediction that $L_i(eq) \propto \nu_i(eq)^{3.1}$, and the fits of the data in Figure 9 give $L_i(eq) \propto \nu_i(eq)^{3.3\pm0.1}$. The spread over such a large range of values for $L_{\nu i}(eq)$, $L_i(eq)$, and $\nu_i(eq)$ can thus be explained by this systematic effect. On the other hand, the errors in Figures 8 & 9 are quite large, and all the $L_{\nu i}(eq)$ and $L_i(eq)$ are still consistent with each other.

It is interesting to note that $I_\nu(eq) \propto \nu_i(eq)^{2.2\pm0.1}$ and $I_\nu(IC) \propto \nu_i(IC)^{2.0\pm0.1}$ for this sample, where $I_\nu \propto L_{\nu i}/{\theta_d}^2$. This dependence would be expected if these sources were intrinsically similar, have black a body spectrum, and are observed in the Rayleigh-Jeans size of the black body spectrum. It should be noted that the small dispersion in intrinsic brightness temperatures described above (§2.1) and the fact that I_ν is approximately proportional to ν^2 go hand in hand.

Table 3 lists the mean and standard deviation of the mean for the logarithmic values of $L_{\nu o}$, L_o, $L_{\nu i}(eq)$, $L_i(eq)$, $L_{\nu i}(IC)$, and $L_i(IC)$, for each class of AGN. Comparing $L_{\nu i}(eq)$ to $L_{\nu i}(IC)$ and $L_i(eq)$ to $L_i(IC)$, agreement for each class of source is found within about 2σ. Ranges of intrinsic luminosity densities and intrinsic luminosities for all classes of AGN are $10^{32.4\ to\ 33.1}$ergs s^{-1}Hz^{-1} and $10^{42\ to\ 43}$ergs s^{-1}.

3. DISENTANGLING RELATIVISTIC EFFECTS IN RADIO-LOUD AGN

The effects of relativistic motion can be described by two quantities: the bulk Lorentz factor of the outflow, Γ, and the angle subtended by the outflow direction and the line of sight to the observer, ϕ. Note that the bulk Lorentz factor is determined by the speed of the outflow relative to the speed of light, β, by the familiar equation $\Gamma = 1/\sqrt{1-\beta^2}$.

Two observable quantities which are combinations of Γ and ϕ are the Doppler factor, δ, and the apparent speed projected onto the plane of the sky relative to the speed of light, β_{app}. These are expressed in terms of β and ϕ as

$$\delta = \frac{\sqrt{1-\beta^2}}{1-\beta\cos\phi}, \tag{6}$$

and

$$\beta_{app} = \frac{\beta\sin\phi}{1-\beta\cos\phi}. \tag{7}$$

Equations (6) and (7) can be used to solve for Γ and ϕ in terms of δ and β_{app}, and it can be shown that

$$\Gamma = \frac{\beta_{app}^2 + \delta^2 + 1}{2\delta} \tag{8}$$

and

$$\tan\phi = \frac{2\beta_{app}}{\beta_{app}^2 + \delta^2 - 1} \tag{9}$$

(see GPCM93; Daly, Guerra, & Güijosa 1996). Thus, Γ and ϕ can be estimated for relativistic outflows in AGN, by combining observational estimates of δ and β_{app}. Here δ_{eq} and δ_{IC} are used to estimate δ.

3.1. Apparent Bulk Flow Versus Pattern Flow

It has been suggested that the pattern velocities, the velocities of radio features observed in VLBI proper motion studies, are greater than the bulk velocities, the velocities responsible for the observed Doppler boosting (see, for example, Lind & Blandford 1985). This issue was addressed by GPCM93, who conclude that the data are consistent with pattern velocities equaling bulk velocities for the sources in their sample with observed superluminal motion.

Vermeulen & Cohen (1994, hereafter VC94) examine the equivalence of pattern velocities and bulk velocities in detail using Monte Carlo simulations of a simple model where the angle between the direction of outflow and the line of sight is allowed to vary randomly, but the bulk Lorentz factor is the same in every jet. They find that the pattern Lorentz factor, Γ_p, would have to be about twice the bulk Lorentz factor, Γ_b, in order to be consistent with the data from the GPCM93 sample. They point out, however, that for a broad distribution of bulk Lorentz factors the data are easily consistent with the $\Gamma_p \simeq \Gamma_b$.

It is assumed, here and throughout, that $\Gamma_p \simeq \Gamma_b$, and any departures from this equality are of order unity.

4. ESTIMATES OF BULK LORENTZ FACTORS AND VIEWING ANGLES

4.1. A Subsample with β_{app} Compiled

VC94 compile a list of 66 radio sources with multi-epoch VLBI observations of the internal proper motions. Table 1 in VC94 lists β_{app} for the features in these radio sources. There are 43 sources that overlap the GPCM93 and the VC94 samples, and these sources are examined below in order to estimate Γ and ϕ (§4.2); preliminary results were presented by Daly, Guerra, & Güijosa (1996).

Table 4 lists the 43 sources that overlap the GPCM93 and VC94 samples. Column (1) lists the IAU Name, column (2) lists the common name if it exists, Column (3) gives the redshift listed by VC94, Column (4) lists the β_{app} estimates from VC94, except for 0108+388 where the estimate is based on more recent observations by Taylor, Readhead, & Pearson (1996). When multiple components are listed by VC94, the weighted mean is taken for β_{app}. Figure 12 shows β_{app} versus $(1+z)$ for the 43 sources in the overlapping sample. Columns (5) and (6) give estimates of δ_{eq} and δ_{IC}, respectively, which are discussed in §2.1 above.

4.2. Values for Γ and ϕ

The values of β_{app}, δ_{eq}, and δ_{IC} listed in Table 4 can be used with equations (8) and (9) to produce two sets of estimates for Γ and ϕ. In the cases where only bounds on β_{app} or δ are available, bounds on Γ and ϕ are computed.

Table 5 lists the solutions for Γ and ϕ using the equipartition Doppler factor, called Γ_{eq} and ϕ_{eq}, and using the inverse Compton Doppler factor, called Γ_{IC} and ϕ_{IC}. Columns (1) and (2) list the IAU name and the common name respectively, Column (3) gives the redshift listed by VC94, Columns (4) and (5) list Γ_{eq} and ϕ_{eq} respectively, and columns (6) and (7) list Γ_{IC} and ϕ_{IC} respectively. Both sets of solutions for Γ and ϕ agree within errors for any given source in Table 5.

Table 6 lists the median values of Γ_{eq}, ϕ_{eq}, Γ_{IC}, and ϕ_{IC} for each class of source, excluding those values which are upper or lower bounds. The median values of the equipartition set (Γ_{eq} and ϕ_{eq}) and the inverse Compton set (Γ_{IC} and ϕ_{IC}) of estimates agree well, except for the median Γ_{eq} and Γ_{IC} of the LDQs which are a factor of about two greater in the equipartition case. Note that excluding 3C216 from the LDQs would not significantly change the median values for this category.

Figures 13a & 13b show Γ_{eq} versus ϕ_{eq} with and without errors respectively, and Figures 14a

& 14b show Γ_{IC} versus ϕ_{IC} with and without errors respectively. The figures without errors are shown so that the symbols are more visible to the reader and bounds on Γ and ϕ are denoted by arrows in these figures. Figures 15a & 15b show ϕ_{eq} and Γ_{eq} as functions of $(1+z)$ respectively, and Figures 16a & 16b show ϕ_{IC} and Γ_{IC} as functions of $(1+z)$ respectively.

The median values for both sets of estimates of Γ and ϕ make it possible to compare different classes of AGN in the context of orientation unified models (see discussion in §4.3). A detailed discussion of each set of Γ and ϕ estimates follows in §§4.2.1 & 4.2.2.

4.2.1. Solutions Using the Equipartition Doppler Factor

The eight BL Lacs studied here span a relatively large range of Γ_{eq}; one source has a value of $\Gamma_{eq} = 1.4 \pm 0.2$, and two sources have Γ_{eq} between 40 and 100, although these two sources have large errors on Γ_{eq}. The remaining five BL Lacs have Γ_{eq} between 3 and 6. The values of ϕ_{eq} for BL Lacs span a range from about 0° to about 50°, with six of the eight BL Lacs having $\phi_{eq} \lesssim 20°$.

Seven of the eight CDHPQs have $\phi_{eq} \lesssim 12°$, and at least five of these sources have $\phi_{eq} \lesssim 6°$. Three out of eight CDHPQs have Γ_{eq} between 3 and 10, and two CDHPQs have Γ_{eq} between 20 and 40. Three sources have limits on Γ_{eq} and ϕ_{eq} instead of values (see §2.1). Two of these sources with bounds, 1156+295 (4C 29.45) and 2230+114 (CTA 102), stand out in Figures 13a,b. The bounds on Γ_{eq} for these two sources, $\Gamma_{eq} < 405$ for 1156+295 and $\Gamma_{eq} > 2.8$ for 2230+114, still allow these sources to have Lorentz factor similar to other CDHPQs.

Five CDLPQs have Γ_{eq} between 5 and 10, and three have Γ_{eq} between 15 and 30. The other two sources only have bounds on Γ_{eq}. Eight out of ten CDLPQs have $\phi_{eq} \lesssim 14°$.

The three CDQ-NPIs all have $\Gamma_{eq} < 9$, and have quite different values for ϕ_{eq}. The sources in this small category in reality belong to the CDHPQs or CDLPQs, and may contain both types.

Five LDQs have Γ_{eq} between 10 and 50. These values of Γ_{eq} are larger than the typical values for the other classes of AGN studied here. One source has Γ_{eq} less than 10 (4C 21.35, $\Gamma_{eq} = 2.8 \pm 2.9$), while another has a lower bound $\Gamma_{eq} > 3$. Only one LDQ has ϕ_{eq} less than 15° (3C216), while the other six LDQs have ϕ_{eq} between 15° and 41°. LDQs have the larger values for ϕ_{eq} than most of the BL Lacs, CDQs (HP, LP, and NPI) studied here.

RGs have the largest values and widest range of ϕ_{eq} of all the categories. Four out of seven RGs have $45° < \phi_{eq} < 135°$, which suggests that these sources have outflows that typically lie close to the plane of the sky (see §4.3). RGs also have the lowest Γ_{eq} of all the categories, with at least four RGs having $\Gamma_{eq} < 2$. Note that the radio galaxies in this sample are compact steep spectrum sources or FRI; there are no FRII radio galaxies in this sample.

4.2.2. Solutions Using the Inverse Compton Doppler Factor

The results for Γ_{IC} and ϕ_{IC} are quite similar to those for Γ_{eq} and ϕ_{eq}, and agree well within errors. This agreement is not surprising considering the correlation and agreement found between δ_{IC} and δ_{eq} (see §2.1).

Five out of eight BL Lacs have Γ_{IC} between 3 and 5, while the total range for all BL Lacs is between 1.5 and 60. Seven BL Lacs have $\phi_{IC} < 20°$. Five out of eight CDHPQs have Γ_{IC} between 8 and 16, while the other three have various upper and lower bounds. These same five CDHPQs all have $\phi_{IC} < 10°$. Six out of ten CDLPQs have Γ_{IC} between 3 and 11, and two have Γ_{IC} around 20. Eight CDLPQs have $\phi_{IC} < 14°$. Five out of seven LDQs have Γ_{IC} between 10 and 30, and five LDQs have ϕ_{IC} between 15° and 45°. As in the equipartition case only one LDQ has ϕ_{IC} less than 15°. Three out of seven RGs have ϕ_{IC} between 45° and 90°, and three RGs have $\phi_{IC} > 90°$. At least six RGs have $\Gamma_{eq} < 2$.

4.3. Implications for Orientation Unified Models of AGN

The results presented §4.2 are consistent with an orientation unification scheme for radio-loud AGN (e.g. Antonucci 1993). Common orientation models have a torus or disk of material that absorbs or obscures the broad absorption lines and other non-stellar radiation emitted from the nuclear region of the AGN, and the classification as a radio galaxy occurs if the torus intersects the line of sight from the nuclear region to the observer. The radio jet axis in radio-loud AGN is thought to be more or less perpendicular to the plane of the torus or disk. In such models (e.g. Barthel 1989), RGs, LDQs, and CDQs, are viewed with different angles with respect to the jet axis (ϕ, which is referred to as the viewing angle): radio galaxies have the largest angles ($\phi \gtrsim 45°$), LDQs have smaller angles ($20° \lesssim \phi \lesssim 45°$), and CDQs have the smallest angles ($\phi \lesssim 20°$).

The RGs, LDQs, and CDQs in overlap of the GPCM93 and VC94 samples have estimates of ϕ consistent with this orientation unification scheme. The RGs in this sample have a median ϕ_{eq} of 110° and a median ϕ_{IC} of 81°, which suggests that they have jets that lie close to the plane of the sky. LDQs typically have a median ϕ_{eq} of 26° and a median ϕ_{IC} of 25°. CDLPQs have a median ϕ_{eq} of 7° and a median ϕ_{IC} of 6°, while CDHPQs have a median ϕ_{eq} of 4° and a median ϕ_{IC} of 3°. The median values for CDQ-NPIs are insignificant since only two sources are used to compute them. It is interesting to note that CDHPQs and CDLPQs have similar median ϕ_{eq} and ϕ_{IC}. This suggests that it is intrinsic differences between these two classes of AGN (not viewing angles) that determine the amount of optical polarization observed.

The BL Lacs in this sample cover a wide range of Γ and ϕ, but have viewing angles typically less than 45°. An extension of the orientation model described above assigns BL Lacs to the parent population of FRI (edge-darkened, Fanaroff & Riley 1974) RGs, where BL Lacs are seen at smaller viewing angles and radio selected BL Lacs have smaller angles than X-ray selected BL

Lacs (see Padovani & Urry 1992). The sample of BL Lacs examined here are almost all radio selected. Mkn 421 (1101+384) is the only X-ray selected BL Lac in this sample, but does not stand out against the other BL Lacs in terms of its Γ or ϕ estimates.

The BL Lacs in this sample have a median ϕ_{eq} of 12° and a median ϕ_{IC} of 14°. These results are consistent with the those found by Kollgaard et al. (1996), who estimate the viewing angles for samples of radio selected BL Lacs, X-ray selected BL Lacs, and RGs by comparing the core enhancement relative to the more diffuse radio emission for each class of AGN. Assuming a constant bulk Lorentz factor, they find that their samples of radio selected BL Lacs, X-ray selected BL Lacs, and RGs have average viewing angles of 10°, 20°, and 60° respectively.

CDQs in this sample are centered around a $\Gamma \approx 9$. If it is assumed that the distribution of bulk Lorentz factors for all classes of radio-loud AGN is centered around $\Gamma \approx 9$, then one might naively expect the mean or median Γ for each of class of AGN to similar. Selection biases likely play a role in the composition of the samples studied, and systematic effects can affect the values that can be obtained from the data.

LDQs have median Γ_{eq} and Γ_{IC} that are larger than those for the CDQs, and these two estimates are different almost by a factor of two, yet the mean ratio of $R = \delta_{eq}/\delta_{IC}$ is only about 0.76 for LDQs. This could be caused by the sensitivity of the estimates of Γ to the precise values of β_{app} and δ when these to parameters are close to one (see eq. 8), which is the case for this sample of LDQs. A decrease of δ away from one will cause the corresponding Γ estimate to increase. If the δ estimates of LDQs in this sample are systematically underestimated, then a noticeable systematic increase in the Γ will result, which could be caused by an overestimate of the peak frequency (see eqs. A2 and A1). It is not clear whether this is one of the causes of the larger Γ for LDQs.

The lower Γ for RGs compared other classes of AGN can be explained as follows. RGs will appear in this sample if there cores are bright enough to have VLBI core size data, which occurs if the sources are nearby (like M87 and NGC 6251) or have very bright compact cores. In particular, FRII radio galaxies are missing from this sample since a majority of their cores are not significantly Doppler boosted and they make difficult targets for VLBI. In the unification scheme described above, RGs have viewing angles around 90°. Approximating $\phi \approx 90°$, one finds that $\delta \approx \Gamma^{-1}$ from equation (6). Thus, $\Gamma \approx \delta^{-1}$, and those RGs with smaller Γ will appear in this sample since these RGs will have larger δ and brighter cores. Even if the true distribution of Γ for RGs peaked at around 10, we may only be able to observe RGs with Γ from 1 to 2. It should be noted that RGs in this sample have values of Γ near unity which are in agreement with other evidence that Doppler boosting is not significant in these sources (e.g. Taylor, Readhead, & Pearson 1996).

There are two sources that seem to have viewing angles greater than 90° based on equipartition and inverse Compton Doppler factors. One, 2352+495, has a lower bound on the viewing angle, the other, 0710+439, is greater than 90° at around 3σ. This would suggest that some RGs have observed outflows that are moving away from the observer, and that if there is an outflow moving

toward the observer it must be intrinsically fainter.

BL Lacs have lower values of Γ than the CDQs, with a median Γ_{eq} of 4.2 and a median Γ_{IC} of 5. Since the BL Lacs studied in this paper are almost exclusively radio selected, it would be interesting to compare Γ and ϕ estimates for a sample of X-ray selected BL Lacs. Kollgaard et al. (1996) find that the core enhancements they observe for BL Lacs and RGs, require that $\Gamma > 4.5$, assuming a constant bulk Lorentz factor for all these sources. The estimates of Γ found here are barely consistent with $\Gamma > 4.5$, but a distribution of Lorentz factors may loosen the constraints placed by Kollgaard et al. (1996).

5. DISCUSSION

The two estimates of the Doppler factor for the sample of radio-loud AGN discussed in §2.1 agree with each other on average and provide a means of estimating the intrinsic properties of these sources (e.g. brightness temperatures, luminosities) and the parameters that describe the kinematics of the relativistic bulk flow of the radio emitting plasma. Although the results here are based on rough estimates of the Doppler factor, the average or typical properties of different classes of AGN can be compared.

Care should be taken when using the estimates of Doppler factors and intrinsic properties computed here since systematic errors contribute most of the uncertainty. These systematic errors arise from the simplification that the observed frequencies correspond to the peak of the core emission. Another concern with this sample is completeness. The sample examined here was defined by GPCM93 as those which had VLBI core size data in the literature at that point in time. The sources that enter this sample will have VLBI cores with higher surface brightness than those excluded from the sample; this will favor the brighter (more highly Doppler boosted) and more compact (smaller angular size) cores. GPCM93 warn that this sample is not complete in any statistical sense, and that biases may have a large effect on the content of this sample.

Sources in the first and second Caltech-Jodrell Bank VLBI surveys (CJ1 and CJ2) form a complete flux-limited sample of almost 400 compact radio sources with VLBI measured core sizes (see Henstock et al. 1995, Xu et al. 1995) and some multi-frequency data. Doppler factor estimates for sources from these samples are currently under investigation, including the use of spectra to estimate the peak frequency of core components in order to more accurately compute Doppler factors (Guerra & Daly 1997). Large samples such as these could be used to estimate the Doppler factors and intrinsic properties of different classes of AGN with greater confidence and statistical weight.

The intrinsic brightness temperatures for this sample are estimated using two sets of Doppler factor estimates, δ_{eq} and δ_{IC}, and both histograms of these values are centered around 7.5×10^{10} K (see §2.1). The intrinsic brightness temperatures are similar for different classes of AGN, despite the fact that the observed brightness temperatures are different for different classes of AGN. The

center of the distribution of intrinsic brightness temperatures is a factor of 4 lower than what would be expected if the "inverse Compton catastrophe" played a major role in the observed brightness temperature cutoff, as noted previously by Readhead (1994). This suggests that either a factor of about 4 has not been accounted for in these estimates (e.g. a geometric factor), or that a physical process other than the "inverse Compton catastrophe" is limiting the intrinsic brightness temperature.

Estimates of the intrinsic luminosity density and luminosity depend strongly on the Doppler factor ($L_{\nu i} \propto \delta^{-3}$ and $L_i \propto \delta^{-4}$), and systematic errors are quite large for these estimates. The large scatter of $L_{\nu i}$ and L_i is a cause for concern since it can be attributed to systematic errors introduced by assuming the observed frequencies correspond to the actual peak frequencies of these sources. In any event, these estimates can be compared to the Eddington luminosity for a supposed massive central object. The Eddington luminosity is $L_E = 1.3 \times 10^{44} M_6$ ergs s^{-1} where M_6 is the mass of the central object in units of $10^6 M_\odot$ which gives a range from 10^{44} to 10^{46} ergs s^{-1} for central objects with $M_6 = 1$ to 100. The mean intrinsic luminosity for the sources examined here is around 10^{42} to 10^{43} ergs s^{-1}, while only five objects (3 BL Lacs, 1 LDQ, and 1 RG) have intrinsic luminosities greater than 10^{46} ergs s^{-1} by more than 1σ. This is consistent with the radio luminosity produced being 0.1 to 1 percent of the Eddington luminosity for a central compact object with mass 10^6 to $10^8 M_\odot$.

A subsample of 43 sources have observed proper motions in the plane of the sky and were used by VC94 and others to compute β_{app}. The values of β_{app} for each of these sources can be combined with the Doppler factor estimates to solve for the bulk Lorentz factor, Γ, and the viewing angle, ϕ (see §3). The estimates using the data compiled here are consistent with the orientations unification scheme for AGN (discussed in §4.3), where CDQs have the smallest ϕ ($< 15^\circ$), LDQs have larger ϕ ($15^\circ < \phi < 45^\circ$), and RGs have the largest ϕ ($> 45^\circ$); note that the RGs in this sample are compact steep spectrum sources or FRI.

Selection biases and systematic errors may play a role in these estimates of Γ and ϕ, in particular for LDQs and RGs (see §4.3). The RGs in this sample have lower Γ than the other classes of AGN, which is consistent with the parent population having outflows that lie close to the plane of the sky (i.e. $\phi \sim 90^\circ$) and the flux-limited nature of the sample studied. The LDQs are in a regime where small systematic errors in δ can strongly affect Γ estimates.

The estimates of ϕ and Γ for the BL Lacs in this sample are consistent with the results of Kollgaard et al. (1996) for radio selected BL Lacs (see §4.3). Their estimates of ϕ are based on the core enhancement of radio selected BL Lacs, X-ray selected BL Lacs, and RGs. A sample of X-ray selected BL Lacs with estimates of ϕ and Γ computed as in §4.2 would give a consistency check for both methods.

Marscher (1977) discusses the effect of gradients in magnetic field and density with radius on the relationships between the observed quantities and the important physical parameters in a nonuniform source. The effect on δ_{eq} and δ_{IC} of including inhomogeneities is constant

multiplicative factor from 0.7 to 1.4, and the the functional dependence on observable quantities is identical to the homogeneous case; the form of the inhomogeneity and the parameter choices are discussed by Marscher (1977). It should be noted that the intrinsic brightness temperatures will be changed by the same constant factor, and that inhomogeneities do not account for the factor of 4 in brightness temperature that would allow the inverse Compton catastrophe to play a major role in the brightness temperature distribution (§2.1).

The spherical model for the radio cores of AGN, which is used throughout this paper to compute Doppler factors, may not be as realistic as those models which consider a jet-like geometry. The expression for δ_{IC} in the jet-like case, which is derived by GPCM93, is

$$\delta_{IC}(jet) = [\delta_{IC}(sph)]^{(4+2\alpha)/(3+2\alpha)}\,, \tag{10}$$

where $\delta_{IC}(sph)$ is the expression given by equation (A1). For a value of $\alpha = 0.75$, $\delta_{IC}(jet) = \delta_{IC}(sph)^{1.2}$ which is a power law only slightly greater than unity. The expression for δ_{eq} in the jet-like case is

$$\delta_{eq}(jet) = [\delta_{eq}(sph)]^{(13+2\alpha)/(9+2\alpha)}\,(\sin\phi)^{2/(9+2\alpha)}\left(\frac{\theta_a}{\theta_b}\right)^{1/(9+2\alpha)}\,, \tag{11}$$

where $\delta_{eq}(sph)$ is given by equation (A2), ϕ is the angle subtended by the direction of the outflow and the line of sight, and (θ_a/θ_b) is the ratio of the angular sizes of the major and minor axes (see Appendix for the derivation of this equation). For $\alpha = 0.75$, $\delta_{eq}(jet) \propto (\sin\phi)^{0.19}$, and $\delta_{eq}(jet) \propto (\theta_a/\theta_b)^{0.09}$, which are very weak dependences. The relation between the jet-like and spherical cases of the equipartition Doppler factor is $\delta_{eq}(jet) \propto \delta_{eq}(sph)^{1.4}$ which is a power-law close to unity. The expressions for inverse Compton and equipartition Doppler factors in the jet-like case appear to be quite similar to those in the spherical case. Thus, approximating a spherical geometry for simplicity can still provide useful Doppler factor estimates even if the true geometry of these outflows is more jet-like.

The authors would like to thank Tom Herbig, Alan Marscher, Tony Readhead, Larry Rudnick, David Schramm, Steve Unwin, Lin Wan, and Greg Wellman for helpful discussions. This work was supported in part by the US National Science Foundation, by an NSF Graduate Fellowship, the Independent College Fund of New Jersey, and by a grant from W. M. Wheeler III.

A. Relevant Formulae

For the simple case of a uniform sphere where the synchrotron-emitting particles have a power-law energy distribution and move through a tangled homogeneous magnetic field, the Doppler factor needed to reconcile the predicted and observed X-ray fluxes (Marscher 1987) is

$$\delta_{IC}(sph) = f(\alpha) S_m \left[\frac{\ln(\nu_b/\nu_{op})}{S_x \theta_d^{6+4\alpha} \nu_x^{\alpha} \nu_{op}^{5+3\alpha}}\right]^{1/(4+2\alpha)} (1+z), \tag{A1}$$

where z is the redshift, S_x is the observed X-ray flux density (in Jy) at frequency ν_x (keV), θ_d is the angular diameter of the sources (in mas), ν_b is the synchrotron high-frequency cutoff (assumed to be 10^5 GHz), α is the optically thin spectral index (where the radio flux density $S_\nu \propto \nu^{-\alpha}$), ν_{op} is the observed frequency of the radio peak (in GHz), and $f(\alpha) = 0.08\alpha + 0.14$. The radio flux density in equation (A1), S_m (Jy), is the value obtained by extrapolating the optically thin flux density to the observed peak at ν_{op}. In equation (A1) and throughout this work, $\theta_d = 1.8\theta_{FWHM}$ and $\theta_{FWHM} = \sqrt{\theta_a\theta_b}$ from VLBI observations, where θ_a and θ_b are the angular sizes of the major and minor axes respectively (see Güijosa & Daly 1996).

The equipartition Doppler factor is estimated by assuming the energy density in magnetic field equals the energy density in synchrotron-emitting relativistic particles (Readhead 1994). In the notation used here,

$$\delta_{eq}(sph) = \left(\left[10^3 F(\alpha)\right]^{34}\left[4h/y(z)\right]^2 (1+z)^{15+2\alpha} S_{op}^{16} \theta_d^{-34} \nu_{op}^{2\alpha-35}\right)^{1/(13+2\alpha)}, \tag{A2}$$

where S_{op} is the observed peak flux density and ν_{op} is the observed frequency of the peak. The solutions for $F(\alpha)$ are given by Scott & Readhead (1977), and the solution of interest here is $F(0.75) = 3.4$ since $\alpha = 0.75$ is assumed throughout. The function $y(z) = H_o a_o r(z)/c$ (Peebles 1993) is a dimensionless function of Ω_o, Ω_Λ, and z, and contains the dependence on the coordinate distance to the source. In equation (A2), the Hubble's constant is parameterized as $H_o = 100\ h$ km s^{-1} kpc^{-1}. The dependence of δ_{eq} on cosmology is very weak. For $\alpha = 0.75$, $\delta_{eq} \propto (a_o r(z))^{-0.14} \propto (h/y(z))^{0.14}$ Throughout this paper, $\Omega_o = 0.1$, $\Omega_\Lambda = 0$, and $h = 0.75$ are assumed, where the functional form of $y(z)$ is that derived from equation (13.36) of Peebles (1993). Note that the results of Güijosa & Daly (1996) were obtained assuming an Einstein-de Sitter cosmology ($\Omega_o = 1.0$, $\Omega_\Lambda = 0$) with $h = 1$.

The expression for $\delta_{eq}(jet)$ (eq. 11) can be derived by equating equipartition magnetic field, B_{eq}, to the synchrotron self-absorbed magnetic field, B_{SSA}, as is done when deriving $\delta_{eq}(sph)$ (Readhead 1994). The equipartition magnetic field is given by

$$B_{eq} = (2\ C_{me}\ i_1(\alpha)\ \tau_p^{-1}\ [1 - \exp(-\tau_p)]\ I_p\ {\nu_p}^{\alpha}\ l^{-1})^{2/7} \tag{A3}$$

where C_{me} and i_1 are defined by Leahy (1991), τ_p is the optical depth of the peak of the spectrum (see Scott & Readhead 1977), ν_p is the frequency of the peak as measured in the frame of the synchrotron-emitting plasma, I_p is the peak specific intensity as measured in the plasma frame, l is the line of sight depth as measured in the plasma frame, and α is the optically thin spectral index ($I_\nu \propto \nu^{-\alpha}$). The synchrotron self-absorbed magnetic field is given by

$$B_{SSA} = \left(\frac{\pi}{6}\ \frac{c_1(\alpha)}{c_2(\alpha)}\ \tau_p^2\ [1 - \exp(-\tau_p)]^{-1}\right)^2 I_p^{-2}\ \nu_p^5 \tag{A4}$$

where $c_1(\alpha)$ and $c_2(\alpha)$ are tabulated by Marscher (1977). To simplify these expression we define

$$G_{eq}(\alpha) \equiv (2\ C_{me}\ i_1(\alpha)\ \tau_p^{-1}\ [1 - \exp(-\tau_p)])^{2/7} \tag{A5}$$

so that $B_{eq} = G_{eq}(\alpha)(I_p\, {\nu_p}^{\alpha}\, l^{-1})^{2/7}$, and

$$G_{SSA}(\alpha) \equiv \left(\frac{\pi}{6}\, \frac{c_1(\alpha)}{c_2(\alpha)}\, \tau_p^2\, [1 - \exp(-\tau_p)]^{-1}\right)^2 \tag{A6}$$

so that $B_{SSA} = G_{SSA}(\alpha)\; I_p^{-2}\; \nu_p^5$.

The equation for $\delta_{eq}(sph)$ is derived by setting $B_{eq} = B_{SSA}$, $I_p = S_{op}\; (1+z)^3\; \delta^{-3}\; \theta_d^{-2}$, $\nu_p = \nu_{op}\; (1+z)\; \delta^{-1}$, $l = \theta_d\; a_o r(z)\; (1+z)^{-1}$, and solving for δ. It should be noted that a spherical geometry is assumed when using these expressions for I_p, ν_p, and l (see GPCM93). The result,

$$\delta_{eq}(sph)^{13+2\alpha} = G_{eq}(\alpha)^7\; G_{SSA}(\alpha)^{-7}\; [a_o r(z)]^{-2}\; (1+z)^{15+2\alpha}\; S_{op}^{16}\, \theta_d^{-34}\; \nu_{op}^{2\alpha-35}, \tag{A7}$$

reduces to the equation of Readhead (1994) for the equipartition Doppler factor (see eq. A2).

The equipartition Doppler factor for a jet-like geometry is derived by using the appropriate expressions for this case, which are $I_p = S_{op}\; (1+z)^3\; \delta^{-2-[2\alpha/(5+2\alpha)]}\; \theta_d^{-2}$, $\nu_p = \nu_{op}\; (1+z)\; \delta^{-1+[2/(5+2\alpha)]}$, and $l = \sqrt{\theta_b/\theta_a}\; \theta_d\; a_o r(z)\; (1+z)^{-1}\; \delta^{-1}\; (\sin\phi)^{-1}$, where θ_a and θ_b are angular sizes of the major and minor axes respectively, and ϕ is the outflow angle (see GPCM93). The result using these substitutions is

$$\delta_{eq}(jet)^{9+2\alpha} = G_{eq}(\alpha)^7\; G_{SSA}(\alpha)^{-7}\; [a_o r(z)]^{-2}\; (1+z)^{(15+2\alpha)}\; S_{op}^{16}\, \theta_d^{-34}\; \nu_{op}^{(2\alpha-35)}\; (\sin\phi)^2\; (\theta_a/\theta_b), \tag{A8}$$

which reduces to equation (11).

The brightness temperature, T_B, is a useful quantity to use when discussing radiative processes. The observed brightness temperature at the peak is

$$T_{Bo} = 1.77 \times 10^{12} \frac{S_{op}}{\theta_d^2 \nu_{op}^2} \tag{A9}$$

(e.g. Readhead 1994). The intrinsic brightness temperature, T_{Bi}, can be related to the observed brightness temperature for a relativistic moving sphere using $T_{Bi} = T_{Bo}(1+z)/\delta$, where z is the redshift to the source and δ is the Doppler factor. These estimates are given by:

$$T_{Bi} = 1.77 \times 10^{12} \frac{S_{op}}{\theta_d^2 \nu_{op}^2} \frac{(1+z)}{\delta} \tag{A10}$$

(e.g. Readhead 1994). Estimates of T_{Bi} using δ_{eq} are denoted $T_{Bi}(eq)$, and those using δ_{IC} are denoted $T_{Bi}(IC)$.

REFERENCES

Antonucci, R. 1993, ARA&A, 31, 473

Barthel, P. D. 1989, ApJ, 336, 606

Blandford, R. D. & Rees, M. J. 1978, in Proc. Pittsburgh Conf. on BL Lac Objects, ed. A. N. Wolfe (Pittsburgh Univ. Press), 328

Conway, R. G. 1982, in IAU Symp. 97, Extragalactic Radio Sources, eds. D. S. Heeschen & C. M. Wade (Dordrecht: Reidel), 167

Daly, R. A., Guerra, E. J., & Güijosa, A. 1996, in Energy Transport in Radio Galaxies and Quasars, eds. P. Hardee, A. Bridle, & A. Zensus (San Francisco: ASP Series), 73

Fanaroff, B. L. & Riley, J. M. 1974, MNRAS, 167, 31p

Garrington, S. T., Leahy, J. P., Conway, R. G., & Laing, R. A. 1988, Nature, 331, 147

Ghisellini, G., Padovani, P., Celotti, A., & Maraschi, L. 1993, ApJ, 407, 65 (GPCM93)

Güijosa, A. & Daly, R. A. 1996, ApJ, 461, 600

Guerra, E. J. & Daly, R. A. 1997, ApJ, in preparation

Henstock, D. R., Browne, I. W. A., Wilkinson, P. N., Taylor, G. B., Vermeulen, R. C., Pearson, T. J., & Readhead, A. C. S. 1995, ApJS, 100, 1

Hooimeyer, J. R. A., Schilizzi, R. T., Miley, G. K., & Barthel, P. D. 1992, A&A, 261, 5

Hoyle, F. R. S., Burbidge, G. R., & Sargent, W. L. W. 1966, Nature, 209, 751

Kollgaard, R. I., Palma, C., Laurent-Muehleisen, S. A., & Feigelson, E. D. 1996, ApJ, 465, 115

Laing, R. A. 1988, Nature, 331, 149

Leahy, J. P. 1991, in Beams and Jets in Astrophysics, ed. P. A. Hughes (Cambridge: Cambridge Univ. Press), 128

Lind, K. R. & Blandford, R. D. 1985, ApJ, 295, 358

Marscher, A. P. 1977, ApJ, 216, 244

Marscher, A. P. 1987, in Superluminal Radio Sources, eds. J. A. Zensus & T. J. Pearson (Cambridge: Cambridge Univ. Press), 280

Marscher, A. P. & Broderick, J. J. 1981, ApJ, 249, 406

Marscher, A. P. & Broderick, J. J. 1985, ApJ, 290, 735

Padovani, P. & Urry, C. M. 1992, ApJ, 387, 449

Pearson, T. J. & Zensus, J. A. 1987, in Superluminal Radio Sources, eds. J. A. Zensus & T. J. Pearson (Cambridge: Cambridge Univ. Press), 1

Readhead, A. C. S. 1994, ApJ, 426, 51

Rees, M. J. 1966, Nature, 211, 468

Rees, M. J. 1967, MNRAS, 135, 345

Reid, A., Shone, D. L., Akujor, C. E., Browne, I. W. A., Browne, I. W. A., Murphy, D. W., Pedelty, J., Rudnick, L., & Walsh, D. 1995, A&AS, 110, 213

Scott, M. A. & Readhead, A. C. S. 1977, MNRAS, 180, 539

Taylor, G. B., Readhead, A. C. S., & Pearson, T. J. 1996, ApJ, 463, 95

Vermeulen, R. C. & Cohen, M. H. 1994, ApJ, 430, 467 (VC94)

Xu, W., Readhead, A. C. S., Pearson, T. J., Polatidis, A. G., & Wilkinson, P. N. 1995, ApJS, 99, 297

This preprint was prepared with the AAS LaTeX macros v4.0.

Table 1. Mean Brightness Temperatures

Class	Mean $T_{Bo}/10^{11}$ K	Mean $T_{Bi}(eq)/10^{11}$ K	Mean $T_{Bi}(IC)/10^{11}$ K
All Sources	2.3 ± 0.3	0.87 ± 0.03	0.73 ± 0.03
BL Lacs	2.2 ± 0.6	0.86 ± 0.06	0.75 ± 0.06
CDHPQs	3.5 ± 0.6	0.79 ± 0.03	0.75 ± 0.06
CDLPQs	2.4 ± 0.5	0.89 ± 0.05	0.80 ± 0.09
CDQ-NPIs	0.74 ± 0.24	0.73 ± 0.19	0.51 ± 0.13
LDQs	2.0 ± 1.7	1.0 ± 0.1	0.78 ± 0.08
LDQs−3C216	0.30 ± 0.09	1.1 ± 0.1	0.76 ± 0.08
RGs	0.36 ± 0.10	0.97 ± 0.13	0.65 ± 0.13

Table 2. Mean δ_{eq}, δ_{IC} for True and Reassigned Angular Sizes

Class	No.	True		Reassigned	
		Mean δ_{eq}	Mean δ_{IC}	Mean δ_{eq}	Mean δ_{IC}
All Sources	100	6.0 ± 0.9	5.1 ± 0.6	26 ± 14	9.2 ± 2.4
BL Lacs	27	4.5 ± 1.2	3.4 ± 0.7	12 ± 7	5.8 ± 2.7
CDHPQs	24	9.0 ± 1.5	8.4 ± 1.0	90 ± 56	23 ± 10
CDLPQs	22	6.9 ± 1.5	6.2 ± 1.4	21 ± 12	13 ± 6
CDQ-NPIs	7	5.1 ± 2.2	5.3 ± 1.8	26 ± 18	14 ± 9
LDQs	11	6.1 ± 5.5	3.6 ± 2.9	3.5 ± 2.0	2.0 ± 0.9
LDQs−3C216	10	0.56 ± 0.22	0.66 ± 0.22	0.9 ± 0.5	0.6 ± 0.2
RGs	9	0.55 ± 0.17	0.65 ± 0.14	1.3 ± 0.8	1.1 ± 0.5

Table 3. Mean Luminosity Densities and Luminosities

Class	Mean $\log L_{\nu o}$ $\left(\frac{\text{ergs}}{\text{s Hz}}\right)$	Mean $\log L_o$ $\left(\frac{\text{ergs}}{\text{s}}\right)$	Mean $\log L_{\nu i}(eq)$ $\left(\frac{\text{ergs}}{\text{s Hz}}\right)$	Mean $\log L_i(eq)$ $\left(\frac{\text{ergs}}{\text{s}}\right)$	Mean $\log L_{\nu i}(IC)$ $\left(\frac{\text{ergs}}{\text{s Hz}}\right)$	Mean $\log L_i(IC)$ $\left(\frac{\text{ergs}}{\text{s}}\right)$
All Sources	33.6 ± 0.1	43.3 ± 0.1	32.9 ± 0.2	42.7 ± 0.3	32.6 ± 0.2	42.2 ± 0.2
BL Lacs	32.8 ± 0.2	42.4 ± 0.2	32.8 ± 0.5	42.5 ± 0.7	32.6 ± 0.4	42.3 ± 0.5
CDHPQs	34.3 ± 0.1	44.1 ± 0.2	32.0 ± 0.3	41.3 ± 0.4	31.9 ± 0.2	41.1 ± 0.3
CDLPQs	34.4 ± 0.2	44.2 ± 0.3	33.0 ± 0.5	42.6 ± 0.6	32.7 ± 0.3	42.2 ± 0.4
CDQ-NPIs	34.0 ± 0.3	43.8 ± 0.4	32.8 ± 0.7	42.4 ± 0.9	32.5 ± 0.5	42.0 ± 0.7
LDQs	33.2 ± 0.3	43.0 ± 0.3	34.4 ± 0.8	44.8 ± 1.1	34.0 ± 0.7	44.3 ± 0.9
LDQs−3C216	33.1 ± 0.3	42.9 ± 0.3	35.0 ± 0.7	45.6 ± 0.9	34.5 ± 0.5	45.0 ± 0.7
RGs	31.9 ± 0.5	41.7 ± 0.5	33.8 ± 1.1	44.3 ± 1.3	33.1 ± 0.7	43.3 ± 0.9

Table 4. The Overlap of the GPCM and VC Samples

Source (1)	Name (2)	z (3)	β_{app} (4)	δ_{eq} (5)	δ_{IC} (6)
BL Lacs					
0454+844	...	0.112	0.9 ± 0.3	1.3	2.4
0851+202	OJ 287	0.306	4.0 ± 0.4	11	6.8
1101+384	Mkn 421	0.031	2.50 ± 0.04	2.2	0.92
1308+326	...	0.996	18 ± 9	4.0	5.2
1749+701	...	0.770	10 ± 1	0.6	0.9
1803+784	...	0.684	0.1 ± 0.9	5.3	6.6
2007+776	...	0.342	3.4 ± 0.7	2.8	3.6
2200+420	BL Lac	0.069	4.6 ± 0.2	5.0	3.4
CDHPQ					
0212+735	...	2.370	8 ± 4	5.1	7.1
0234+285	CTD 20	1.213	16 ± 8	6.6	13
1156+295	4C 29.45	0.729	41 ± 2	> 2.1	> 4.9
1253−055	3C 279	0.538	3.7 ± 0.5	13.2	14.0
1641+399	3C 345	0.595	9.6 ± 0.2	1.4	4.1
2223−052	3C 446	1.404	0.0 ± 3.6	16.6	16.0
2230+114	CTA 102	1.037	0 ± 24	> 0.9	> 1.5
2251+158	3C 454.4	0.859	3.2 ± 0.6	> 5.2	> 4.6
CDLPQ					
0016+731	...	1.781	16 ± 4	5.2	7.9
0153+744	...	2.340	1.9 ± 3.5	> 1.3	> 1.8
0333+321	NRAO 140	1.258	8.3 ± 0.5	27	13.0
0430+052	3C 120	0.033	4.7 ± 0.5	> 11	> 4.1
0552+398	DA 193	2.365	3.6 ± 1.8	1.1	2.2
0711+356	OI 318	1.620	0.0 ± 1.7	20	6.4
0836+710	4C 71.07	2.170	16 ± 3	7.7	6.7
0923+392	4C 39.25	0.699	6.2 ± 0.3	6.5	8.9
1226+023	3C 273	0.158	8.8 ± 0.2	7.9	4.6
1928+738	4C 73.18	0.302	6.8 ± 0.3	3.2	3.4
CDQ-NPI					
0615+820	...	0.710	1.7 ± 1.7	0.7	1.4
1039+811	...	1.260	< 4	16.6	12.2
1150+812	...	1.250	6 ± 3	8.2	9.6

Table 4—Continued

Source (1)	Name (2)	z (3)	β_{app} (4)	δ_{eq} (5)	δ_{IC} (6)
LDQ					
0850+581	4C 58.17	1.322	7 ± 1	2.2	2.5
0906+430	3C 216	0.670	6 ± 1	61	33
1040+123	3C 245	1.029	5.2 ± 2.5	0.5	1.4
1222+216	4C 21.35	0.435	2.1 ± 0.9	1.2	1.0
1618+177	3C 334	0.555	2.8 ± 0.9	> 0.2	> 0.3
1721+343	4C 34.47	0.206	2.9 ± 0.3	0.1	0.2
1830+285	4C 28.45	0.594	3.9 ± 0.8	0.4	0.4
RG					
0108+388	OC 314	0.669	0.90 ± 0.25	0.2	0.7
0316+413	3C 84	0.018	0.6 ± 0.1	1.2	1.2
0710+439	...	0.518	0.1 ± 0.2	0.2	0.4
1228+127	M 87	0.004	0.2 ± 0.1	0.8	0.8
1637+826	NGC 6251	0.023	0.1 ± 0.1	> 1.3	> 1.0
2021+614	OW 637	0.227	0.3 ± 0.3	0.9	1.1
2352+495	OZ 488	0.237	< 0.4	0.3	0.5

Table 5. Solutions for Γ and ϕ

Source (1)	Name (2)	z (3)	Γ_{eq} (4)	ϕ_{eq}(deg) (5)	Γ_{IC} (6)	ϕ_{IC}(deg) (7)
BL Lacs						
0454+844	...	0.112	1.4 ± 0.2	48 ± 97	1.6 ± 0.8	18 ± 35
0851+202	OJ 287	0.306	6 ± 8	3 ± 9	5 ± 2	7 ± 11
1101+384	Mkn 421	0.031	3 ± 1	26 ± 34	5 ± 4	39 ± 7
1308+326	...	0.996	42 ± 72	6 ± 3	33 ± 40	6 ± 3
1749+701	...	0.770	83 ± 133	12 ± 1	56 ± 56	12 ± 1
1803+784	...	0.684	3 ± 4	0.6 ± 4.5	3 ± 3	0.4 ± 2.6
2007+776	...	0.342	3.6 ± 1.6	21 ± 26	3.5 ± 0.7	16 ± 17
2200+420	BL Lac	0.069	4.7 ± 0.4	12 ± 20	5.0 ± 1.6	16 ± 11
CDHPQ						
0212+735	...	2.370	9 ± 9	10 ± 10	8 ± 5	8 ± 7
0234+285	CTD 20	1.213	23 ± 32	6 ± 4	16 ± 10	4 ± 3
1156+295	4C 29.45	0.729	< 405	< 2.8	< 175	< 2.8
1253−055	3C 279	0.538	7 ± 10	2 ± 7	7.5 ± 6.5	2 ± 4
1641+399	3C 345	0.595	34 ± 52	12 ± 1	13 ± 9	10 ± 3
2223−052	3C 446	1.404	8 ± 13	0.0 ± 1.5	8 ± 8	0.0 ± 1.6
2230+114	CTA 102	1.037	> 1.0	0 ± 180	> 1.1	0 ± 180
2251+158	3C 454.4	0.859	> 3.7	< 10	> 3.5	< 12
CDLPQ						
0016+731	...	1.781	27 ± 36	7 ± 2	20 ± 14	6 ± 2
0153+744	...	2.340	> 2.1	< 42	> 2.1	< 33
0333+321	NRAO 140	1.258	15 ± 20	1 ± 4	9 ± 4	4 ± 6
0430+052	3C 120	0.033	> 6	< 4	> 4.5	< 14
0552+398	DA 193	2.365	7 ± 11	29 ± 14	4.2 ± 3.5	23 ± 13
0711+356	OI 318	1.620	10 ± 16	0 ± 1	3 ± 3	0 ± 5
0836+710	4C 71.07	2.170	19 ± 20	6 ± 4	21 ± 16	6 ± 2
0923+392	4C 39.25	0.699	6.3 ± 0.5	9 ± 15	6.6 ± 2.3	6 ± 8
1226+023	3C 273	0.158	8.9 ± 1.5	7 ± 10	11 ± 6	10 ± 4
1928+738	4C 73.18	0.302	8.9 ± 9.1	14 ± 8	8.6 ± 5.2	14 ± 5
CDQ-NPI						
0615+820	...	0.710	3 ± 6	54 ± 42	2 ± 2	41 ± 31
1039+811	...	1.260	< 8.8	< 1.5	< 6.7	< 2.7
1150+812	...	1.250	6 ± 4	7 ± 14	7 ± 3	5 ± 8

Table 5—Continued

Source (1)	Name (2)	z (3)	Γ_{eq} (4)	ϕ_{eq}(deg) (5)	Γ_{IC} (6)	ϕ_{IC}(deg) (7)
LDQ						
0850+581	4C 58.17	1.322	12 ± 16	15 ± 5	11 ± 10	15 ± 4
0906+430	3C 216	0.670	31 ± 49	0.2 ± 0.6	17 ± 16	0.6 ± 1.2
1040+123	3C 245	1.029	28 ± 51	22 ± 10	11 ± 13	21 ± 9
1222+216	4C 21.35	0.435	2.8 ± 2.9	41 ± 30	3.2 ± 2.9	44 ± 18
1618+177	3C 334	0.555	> 3	< 39	> 3	< 39
1721+343	4C 34.47	0.206	46 ± 74	38 ± 4	32 ± 32	38 ± 4
1830+285	4C 28.45	0.594	20 ± 32	29 ± 6	21 ± 23	29 ± 6
RG						
0108+388	OC 314	0.669	4 ± 6	94 ± 17	1.7 ± 1.0	81 ± 32
0316+413	3C 84	0.018	1.15 ± 0.07	60 ± 160	1.15 ± 0.08	56 ± 99
0710+439	...	0.518	2.6 ± 3.9	170 ± 25	1.5 ± 1.1	170 ± 30
1228+127	M 87	0.004	1.0 ± 0.4	120 ± 180	1.1 ± 0.3	130 ± 90
1637+826	NGC 6251	0.023	> 1.1	< 15	> 1.0	< 88
2021+614	OW 637	0.227	1.1 ± 0.3	110 ± 180	1.04 ± 0.09	60 ± 180
2352+495	OZ 488	0.237	< 1.8	> 133	< 1.25	> 124

Table 6. Median Values of Γ and ϕ

Class	Med. Γ_{eq}	Med. ϕ_{eq}(deg)	Med. Γ_{IC}	Med. ϕ_{IC}(deg)
BL Lacs	4.2 ± 0.7	12 ± 4	5.0 ± 0.8	14 ± 2
CDHPQ	9 ± 1	4 ± 2	8 ± 1	3.0 ± 1.5
CDLPQ	9.5 ± 1.2	7 ± 2	8.8 ± 1.7	6 ± 1
CDQ-NPI	4.5 ± 1.5	30 ± 23	4.5 ± 2.5	23 ± 18
LDQ	24 ± 5	26 ± 6	14 ± 3	25 ± 6
RG	1.15 ± 0.08	110 ± 9	1.15 ± 0.06	81 ± 14

Fig. 1.— (a) The equipartition Doppler factor, δ_{eq}, vs. $(1+z)$; (b) the inverse Compton Doppler factor, δ_{IC}, vs. $(1+z)$ for the 100 sources in this study. Symbols: solid circles are BL Lacs, solid diamonds are CDHPQs, solid squares are CDLPQs, solid triangles are CDQ-NPIs, open diamonds are LDQs, and open squares are RGs.

Fig. 2.— The distribution of equipartition Doppler factors, δ_{eq} (dotted line), and inverse Compton Doppler factors, δ_{IC} (dashed line), for all sources in this study.

Fig. 3.— The distribution of equipartition Doppler factors, δ_{eq} (dotted line), and inverse Compton Doppler factors, δ_{IC} (dashed line), for each class of AGN: (a) BL Lacs, (b) CDHPQs, (c) CDLPQs, (d) CDQ-NPIs, (e) LDQs, (f) RGs.

Fig. 4.— The distribution of observed brightness temperatures, T_{Bo} (solid line), and intrinsic brightness temperatures, $T_{Bi}(eq)$ (dotted line) & $T_{Bi}(IC)$ (dashed line), for all sources in this study.

Fig. 5.— The distribution of observed brightness temperatures, T_{Bo} (solid line), and intrinsic brightness temperatures, $T_{Bi}(eq)$ (dotted line) & $T_{Bi}(IC)$ (dashed line), for each class of AGN: (a) BL Lacs, (b) CDHPQs, (c) CDLPQs, (d) CDQ-NPIs, (e) LDQs, (f) RGs.

Fig. 6.— The uncorrected luminosity density, $L_{\nu_{un}}$, vs. $(1+z)$ for all 100 sources. Symbols: solid circles are BL Lacs, solid diamonds are CDHPQs, solid squares are CDLPQs, solid triangles are CDQ-NPIs, open diamonds are LDQs, and open squares are RGs.

Fig. 7.— The uncorrected luminosity , L_{un}, vs. $(1+z)$ for all 100 sources. Symbols: solid circles are BL Lacs, solid diamonds are CDHPQs, solid squares are CDLPQs, solid triangles are CDQ-NPIs, open diamonds are LDQs, and open squares are RGs.

Fig. 8.— The intrinsic luminosity density $L_{\nu i}(eq)$ vs. the rest frame frequency $\nu_i(eq)$. The result of a power law fit is $L_{\nu i}(eq) \propto \nu_i(eq)^{2.3\pm0.1}$ with a reduced χ^2 equal to 4.6 and a correlation coefficient $r = 0.91$. Symbols: solid circles are BL Lacs, solid diamonds are CDHPQs, solid squares are CDLPQs, solid triangles are CDQ-NPIs, open diamonds are LDQs, and open squares are RGs.

Fig. 9.— The intrinsic luminosity $L_i(eq)$ vs. the rest frame frequency $\nu_i(eq)$. The result of a power law fit is $L_i(eq) \propto \nu_i(eq)^{3.3\pm0.1}$ with a reduced χ^2 equal to 4.0 and a correlation coefficient $r = 0.96$. Symbols: solid circles are BL Lacs, solid diamonds are CDHPQs, solid squares are CDLPQs, solid triangles are CDQ-NPIs, open diamonds are LDQs, and open squares are RGs.

Fig. 10.— The intrinsic luminosity density $L_{\nu i}(eq)$ vs. $(1+z)$. The result of a power law fit is $L_{\nu i}(eq) \propto (1+z)^{2.5\pm1.6}$ with a reduced χ^2 equal to 1.3 and a correlation coefficient $r = 0.16$. Symbols: solid circles are BL Lacs, solid diamonds are CDHPQs, solid squares are CDLPQs, solid triangles are CDQ-NPIs, open diamonds are LDQs, and open squares are RGs.

Fig. 11.— The intrinsic luminosity $L_i(eq)$ vs. $(1+z)$. The result of a power law fit is

$L_{\nu i}(eq) \propto (1+z)^{0.9\pm 2.2}$ with a reduced χ^2 equal to 1.4 and a correlation coefficient $r = 0.04$. Symbols: solid circles are BL Lacs, solid diamonds are CDHPQs, solid squares are CDLPQs, solid triangles are CDQ-NPIs, open diamonds are LDQs, and open squares are RGs.

Fig. 12.— The apparent speed in the plane of the sky, β_{app}, vs. redshift, z for the overlap of the GPCM93 and VC94 samples (upper bounds are indicated by arrows). Symbols: solid circles are BL Lacs, solid diamonds are CDHPQs, solid squares are CDLPQs, solid triangles are CDQ-NPIs, open diamonds are LDQs, and open squares are RGs.

Fig. 13.— Γ_{eq} vs. ϕ_{eq}, estimates using the equipartition Doppler factor for the overlap of the GPCM93 and VC94 samples (upper and lower bounds indicated by arrows): (a) with errors shown, and (b) without errors shown. Symbols: solid circles are BL Lacs, solid diamonds are CDHPQs, solid squares are CDLPQs, solid triangles are CDQ-NPIs, open diamonds are LDQs, and open squares are RGs.

Fig. 14.— Γ_{IC} vs. ϕ_{IC}, estimates using the inverse Compton Doppler factor for the overlap of the GPCM93 and VC94 samples (upper and lower bounds indicated by arrows): (a) with errors shown, and (b) without errors shown.

Fig. 15.— (a) ϕ_{eq} and (b) Γ_{eq} as functions of $(1+z)$. Symbols: solid circles are BL Lacs, solid diamonds are CDHPQs, solid squares are CDLPQs, solid triangles are CDQ-NPIs, open diamonds are LDQs, and open squares are RGs.

Fig. 16.— (a) ϕ_{IC} and (b) Γ_{IC} as functions of $(1+z)$. Symbols: solid circles are BL Lacs, solid diamonds are CDHPQs, solid squares are CDLPQs, solid triangles are CDQ-NPIs, open diamonds are LDQs, and open squares are RGs.

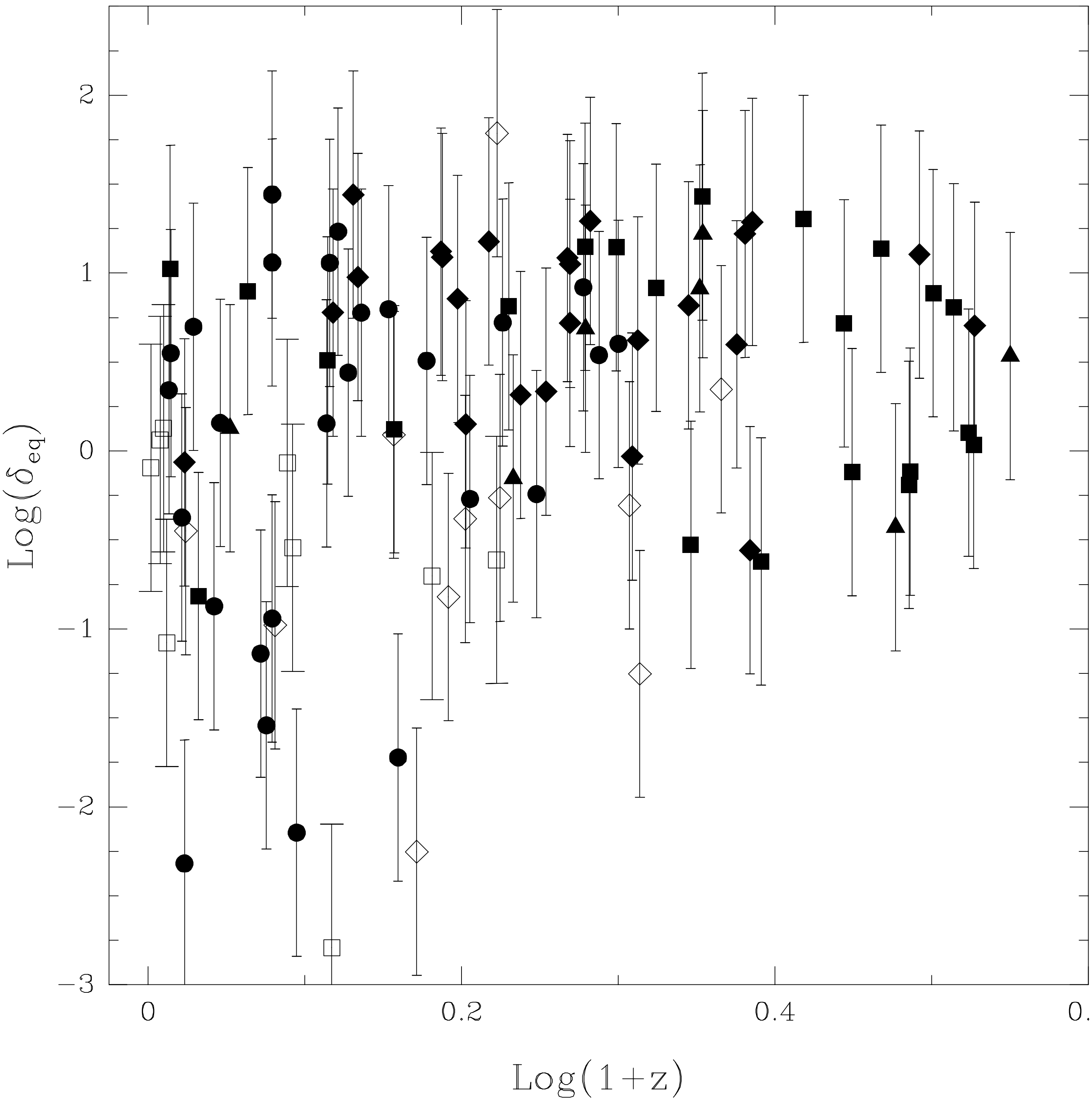

Log(δ_{eq})
Log(1+z)
2
1
0
−1
−2
−3
0
0.2
0.4
0.6

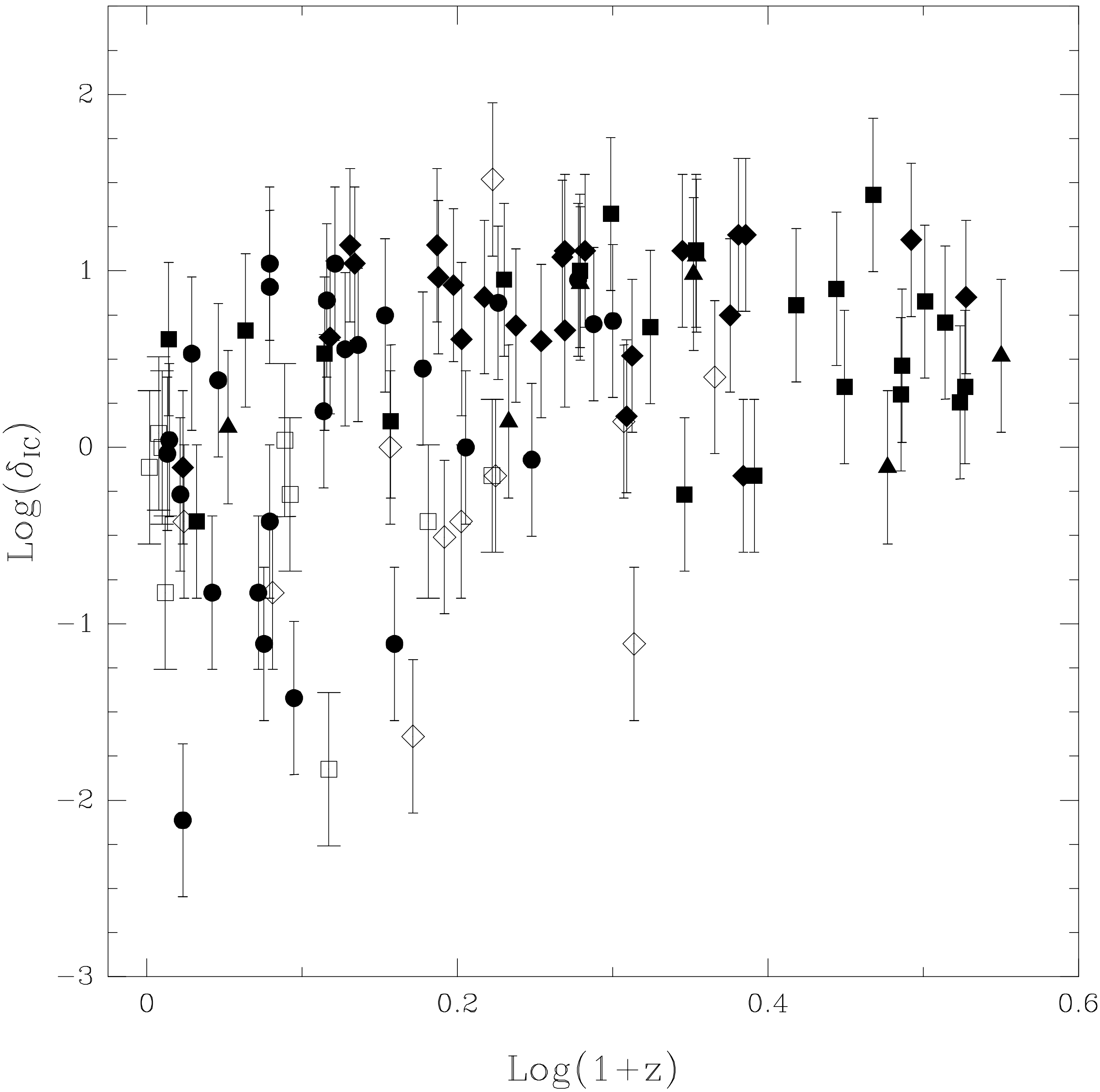

2
1
0
−1
−2
−3
0
0.2
0.4
0.6
Log(δ_{IC})
Log(1+z)

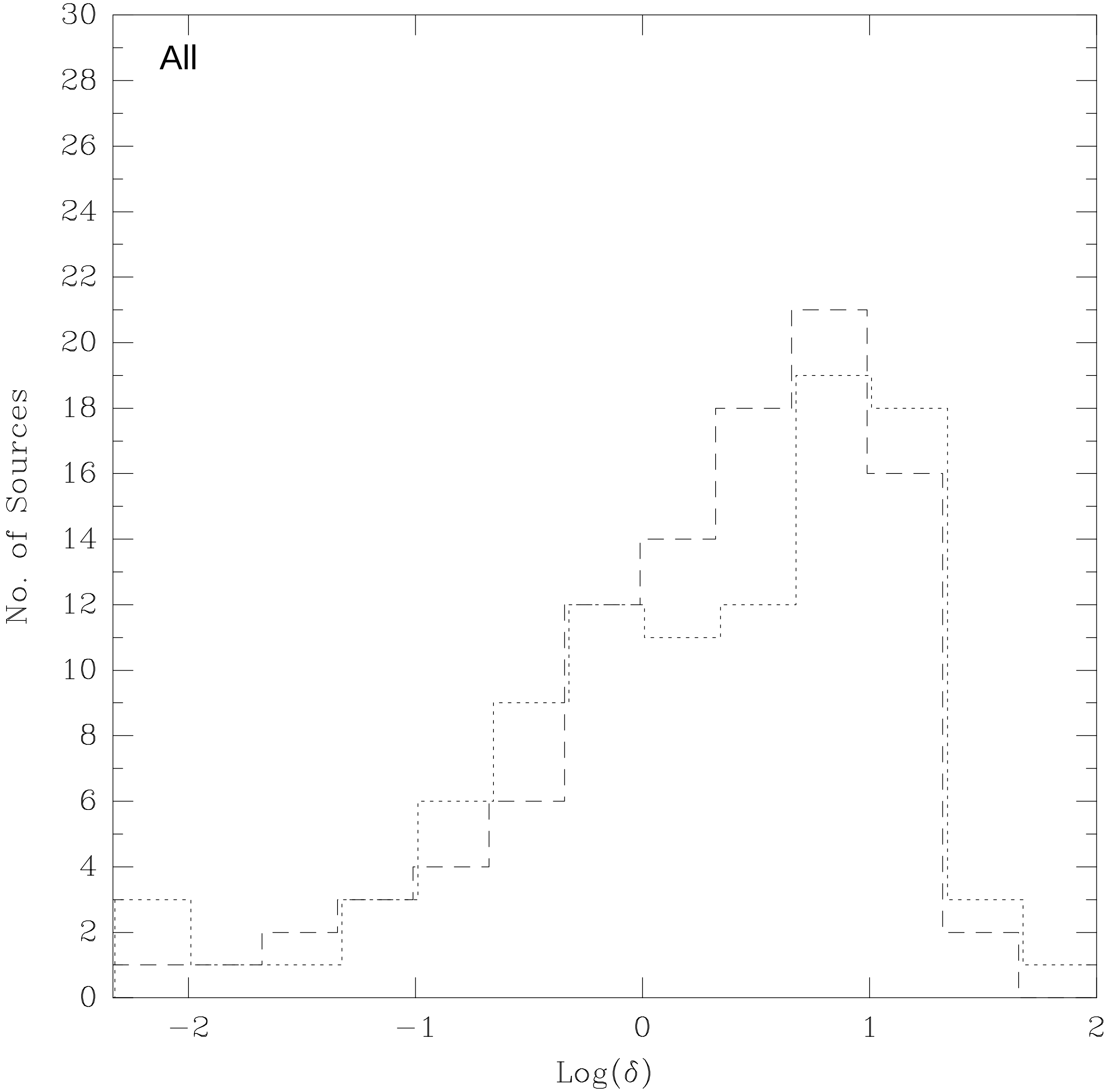

All
No. of Sources
Log(δ)
30
28
26
24
22
20
18
16
14
12
10
8
6
4
2
0
−2
−1
0
1
2

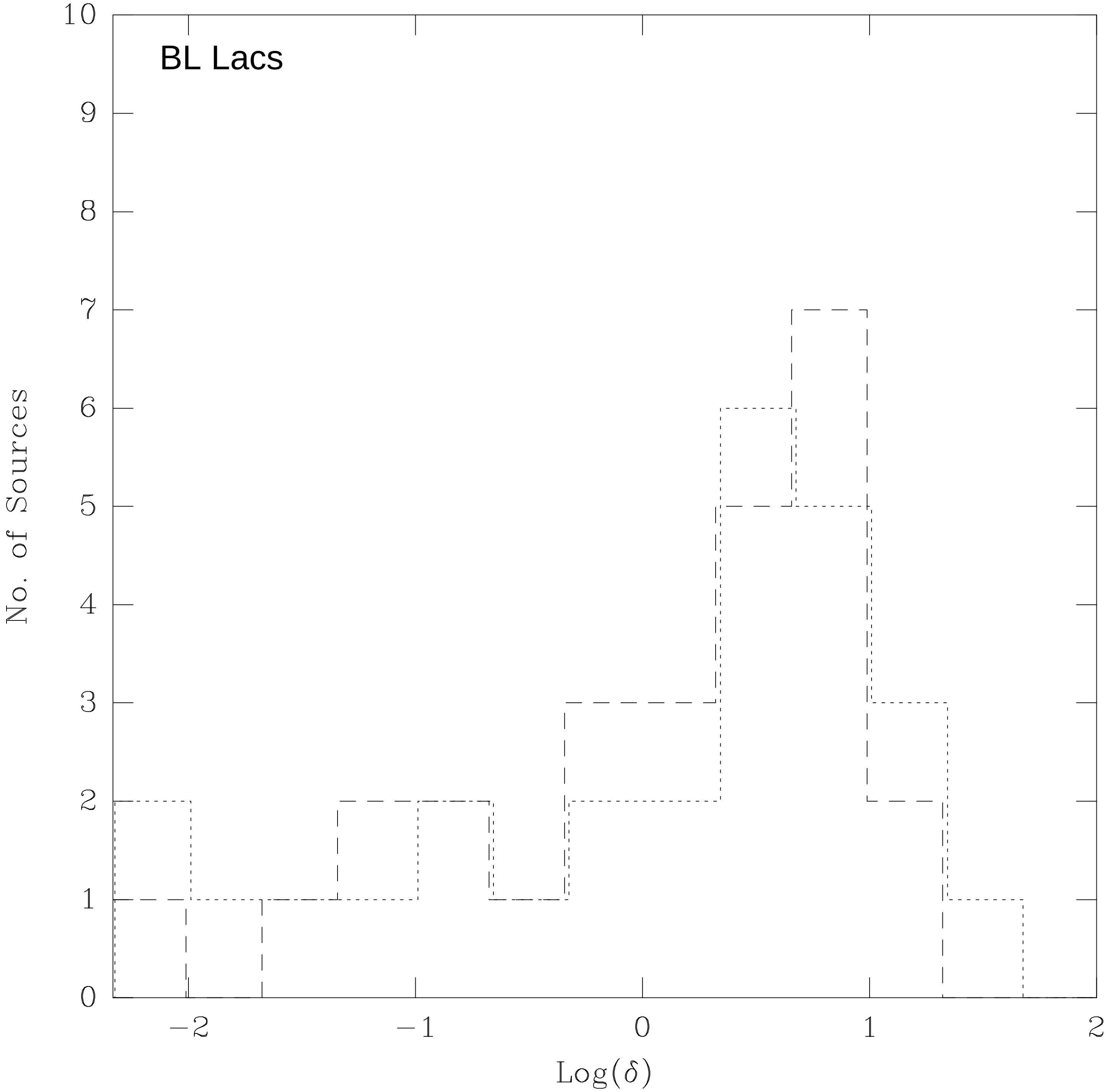
BL Lacs
No. of Sources
Log(δ)
0
1
2
3
4
5
6
7
8
9
10
−2
−1
0
1
2

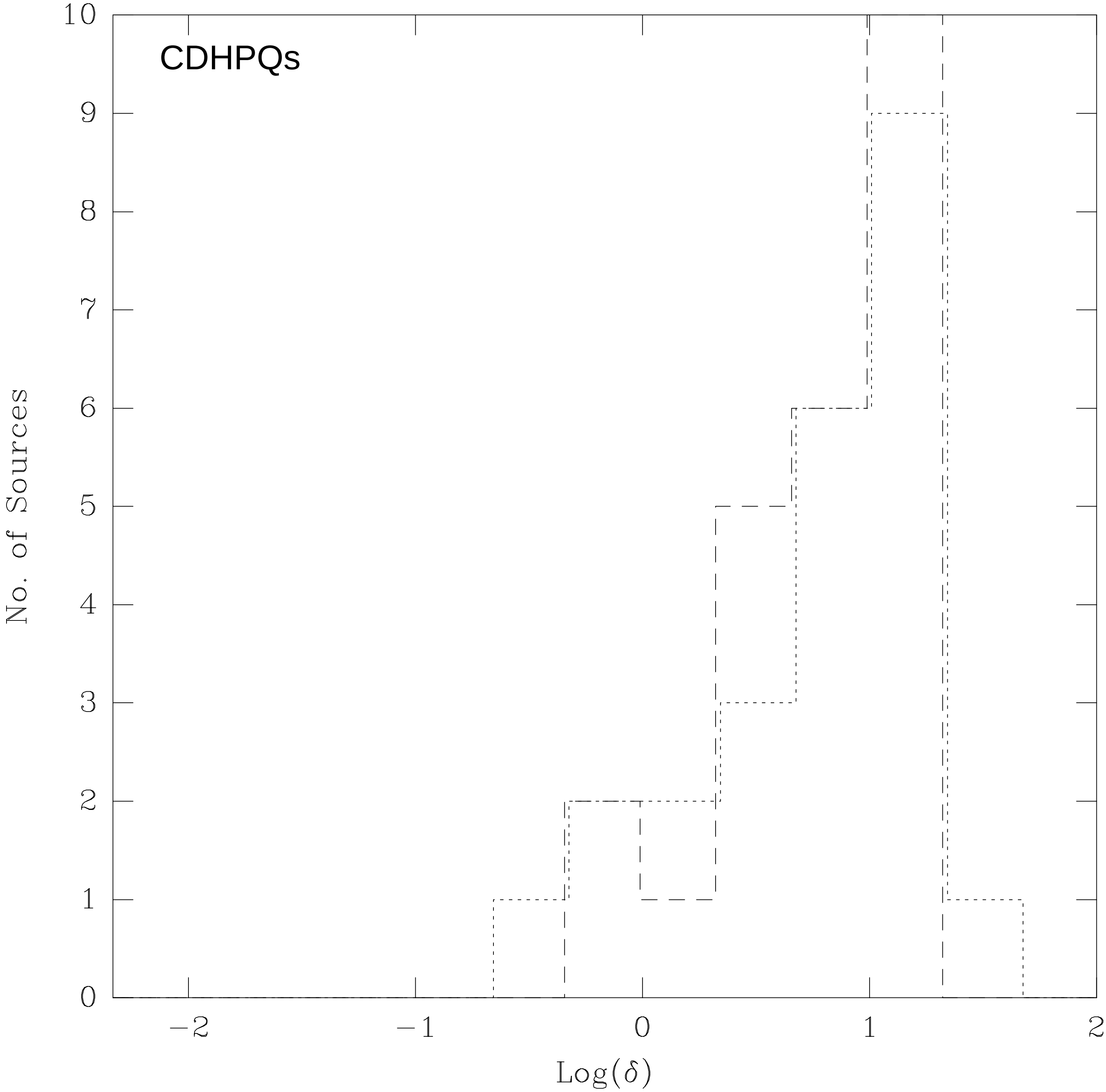
CDHPQs
No. of Sources
Log(δ)
0
1
2
3
4
5
6
7
8
9
10
−2
−1
0
1
2

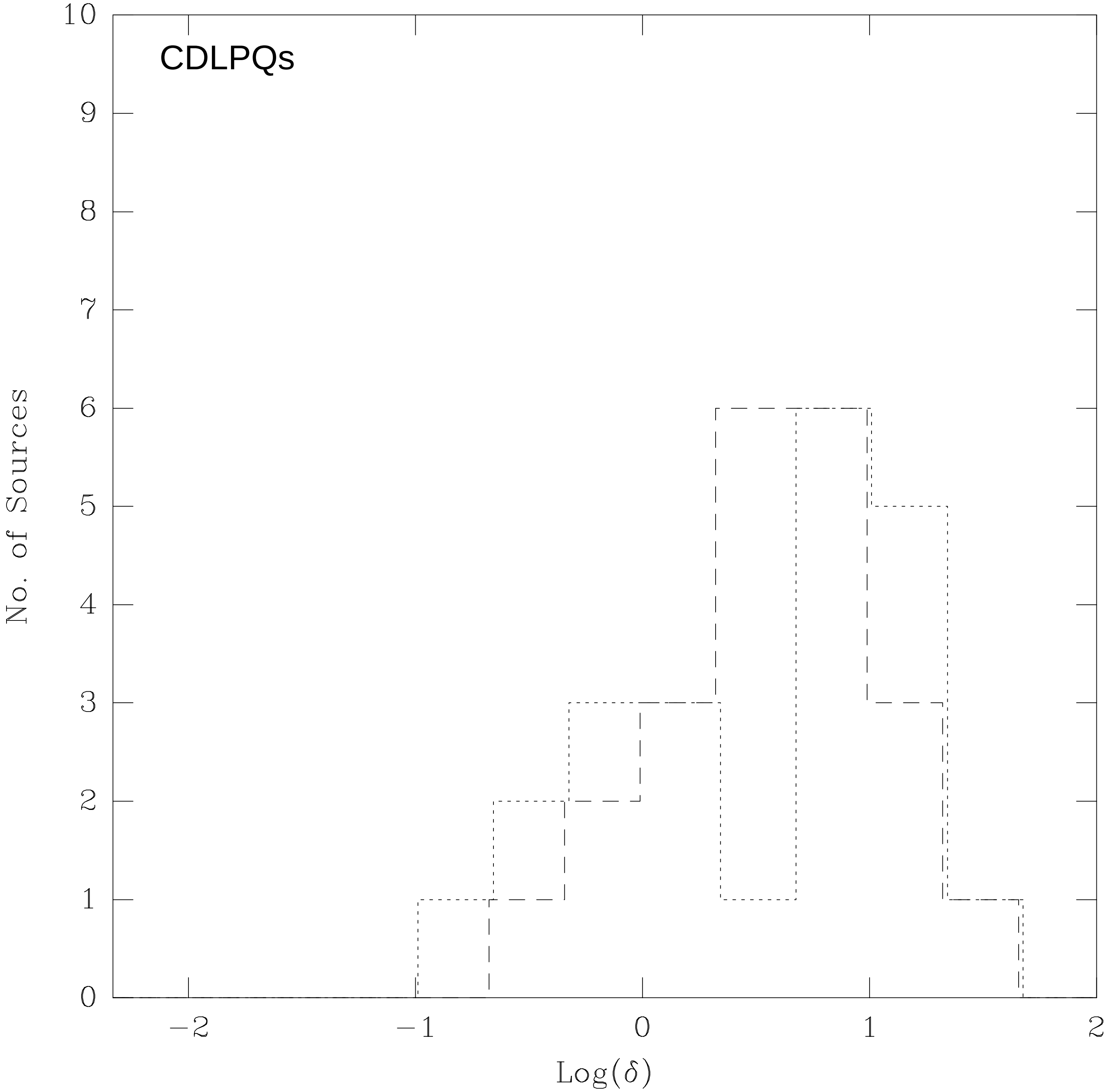

CDLPQs
No. of Sources
Log(δ)
0
1
2
3
4
5
6
7
8
9
10
−2
−1
0
1
2

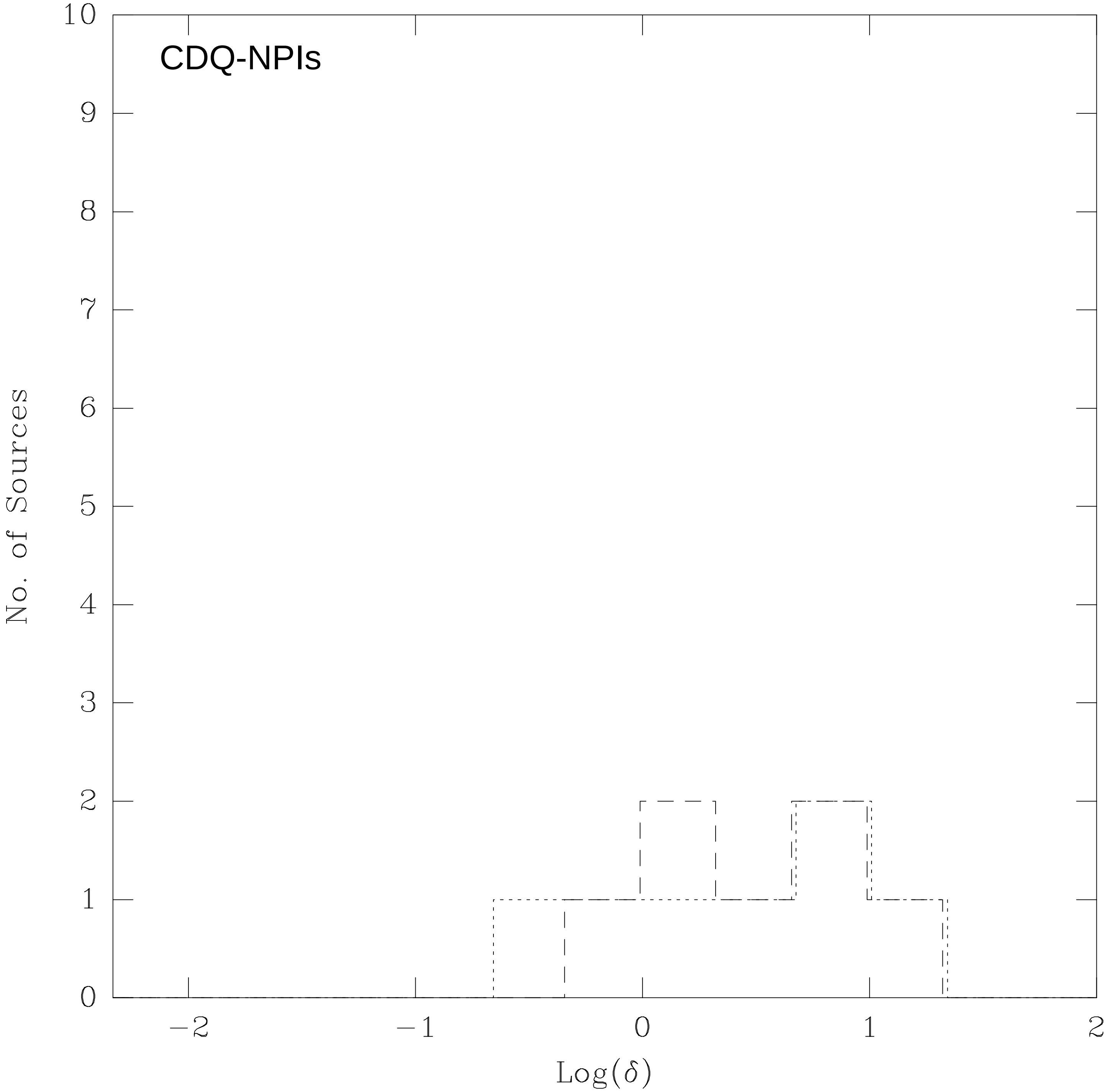
CDQ-NPIs
No. of Sources
Log(δ)
0
1
2
3
4
5
6
7
8
9
10
−2
−1
0
1
2

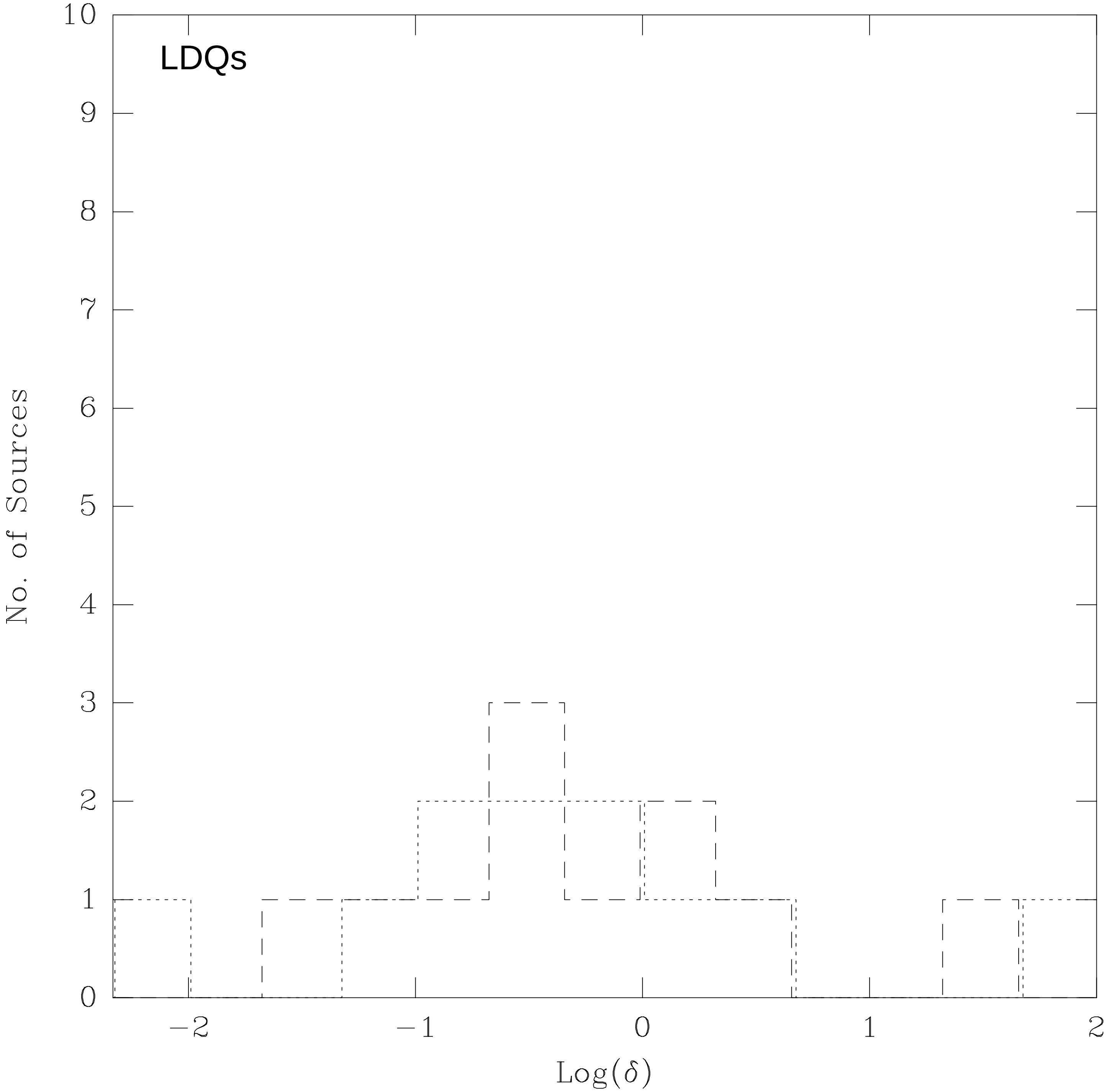

LDQs
No. of Sources
Log(δ)
0
1
2
3
4
5
6
7
8
9
10
−2
−1
0
1
2

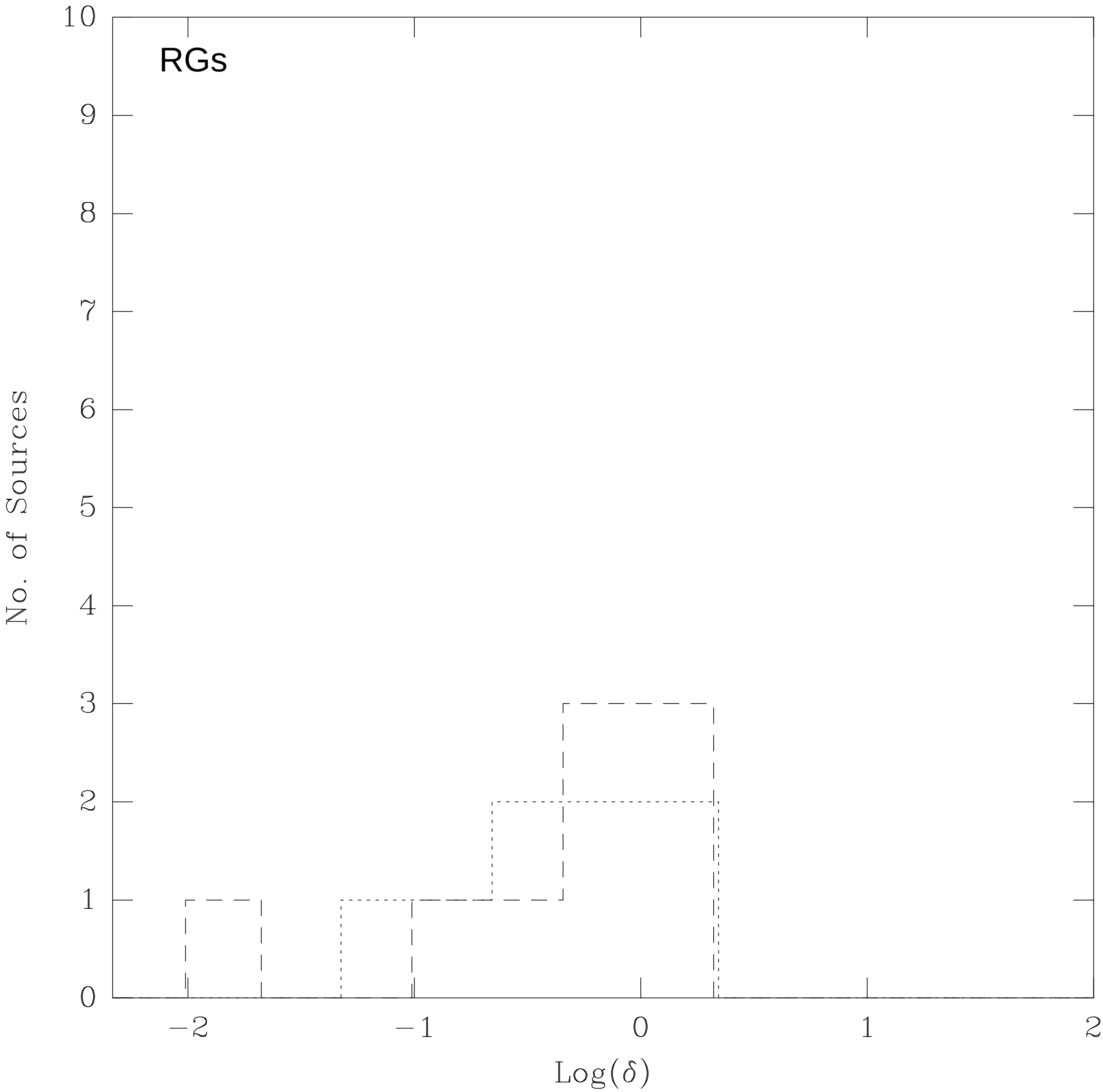
RGs
No. of Sources
Log(δ)
0
1
2
3
4
5
6
7
8
9
10
−2
−1
0
1
2

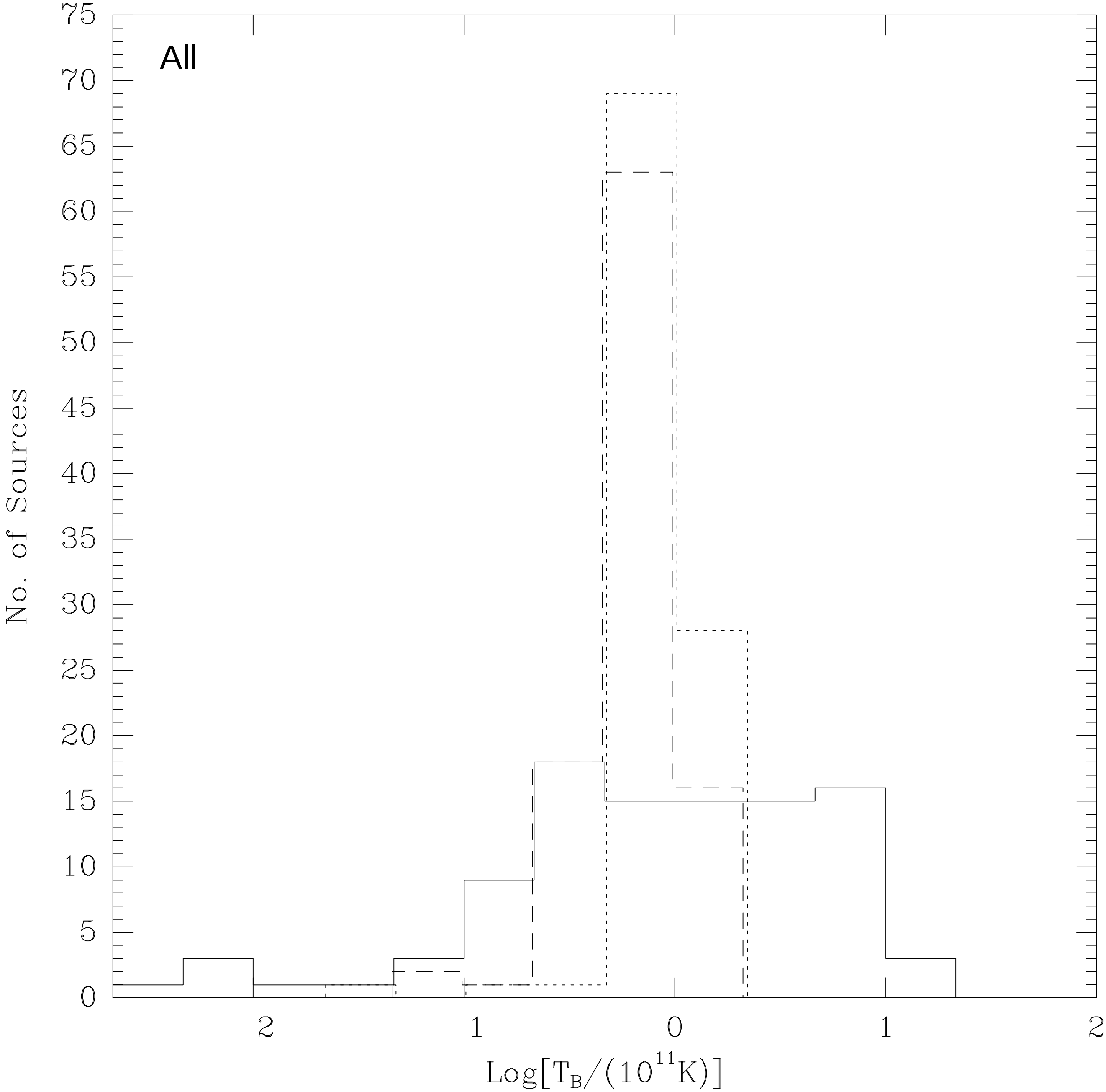
All
No. of Sources
Log[T_B/(10^11 K)]
0
5
10
15
20
25
30
35
40
45
50
55
60
65
70
75
−2
−1
0
1
2

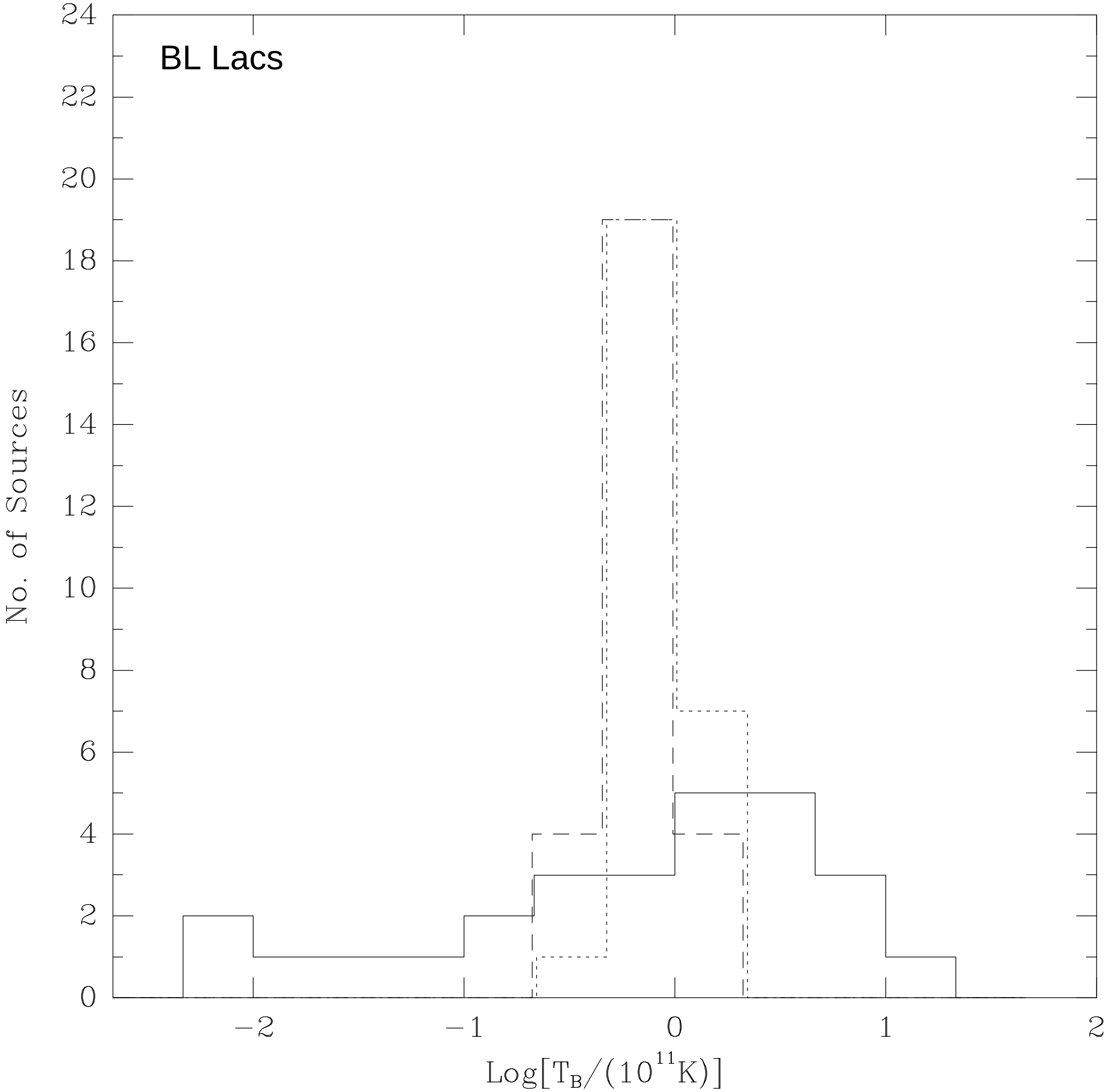
BL Lacs
No. of Sources
Log[T_B/(10^{11}K)]
0
2
4
6
8
10
12
14
16
18
20
22
24
−2
−1
0
1
2

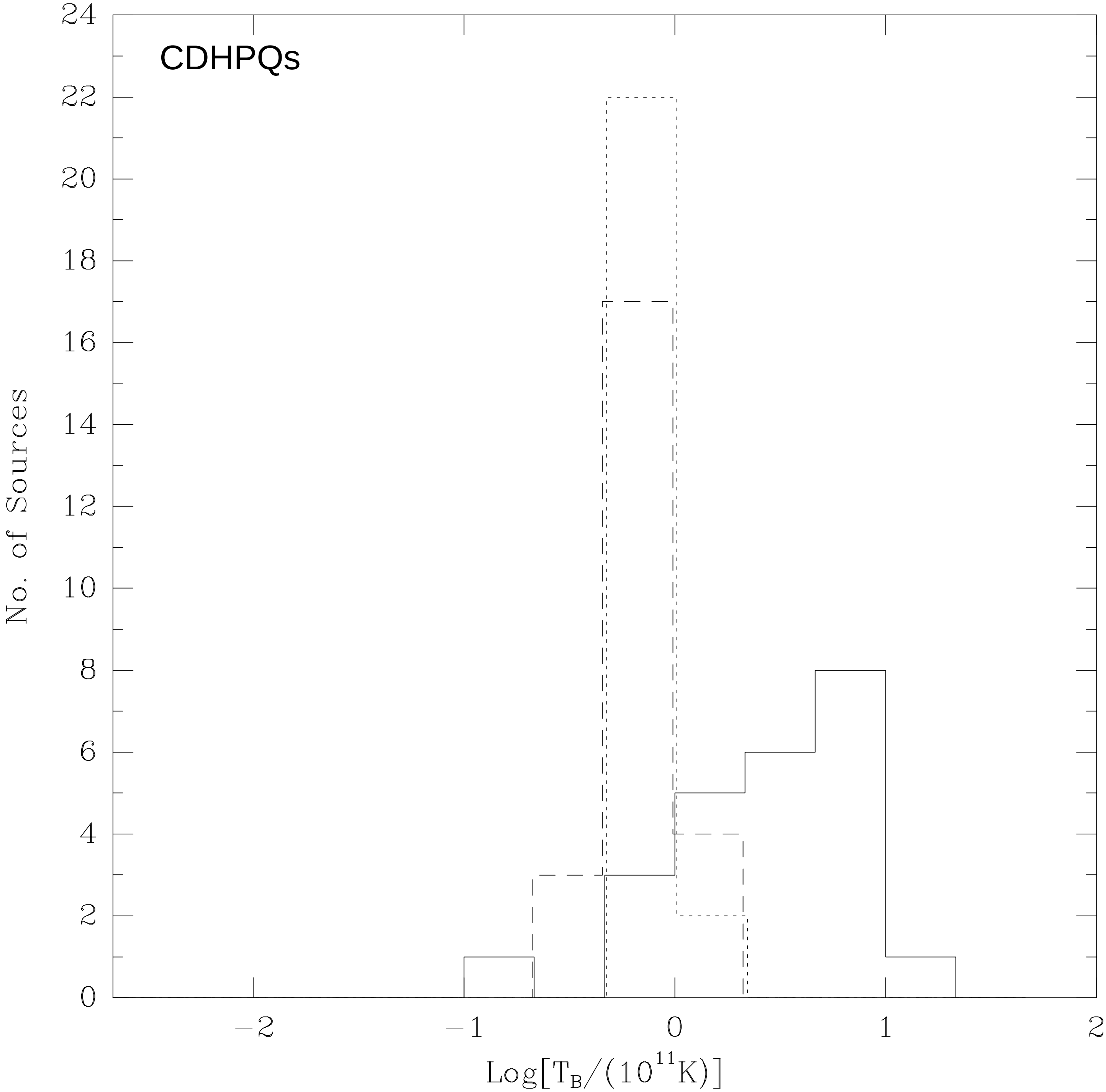
CDHPQs
No. of Sources
Log[T_B/(10^{11}K)]
0
2
4
6
8
10
12
14
16
18
20
22
24
−2
−1
0
1
2

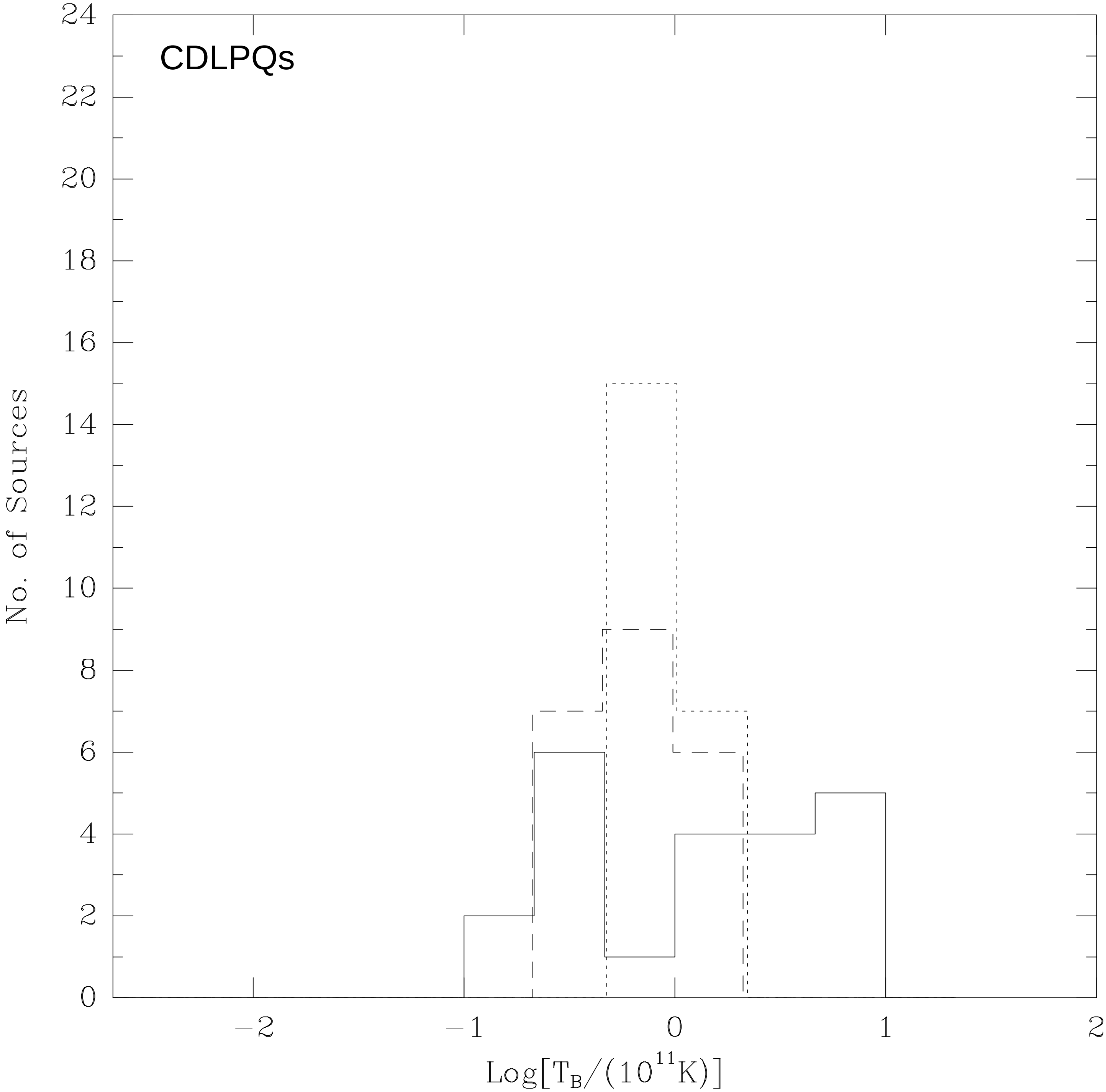
CDLPQs
No. of Sources
Log[T_B/(10^{11}K)]
0
2
4
6
8
10
12
14
16
18
20
22
24
−2
−1
0
1
2

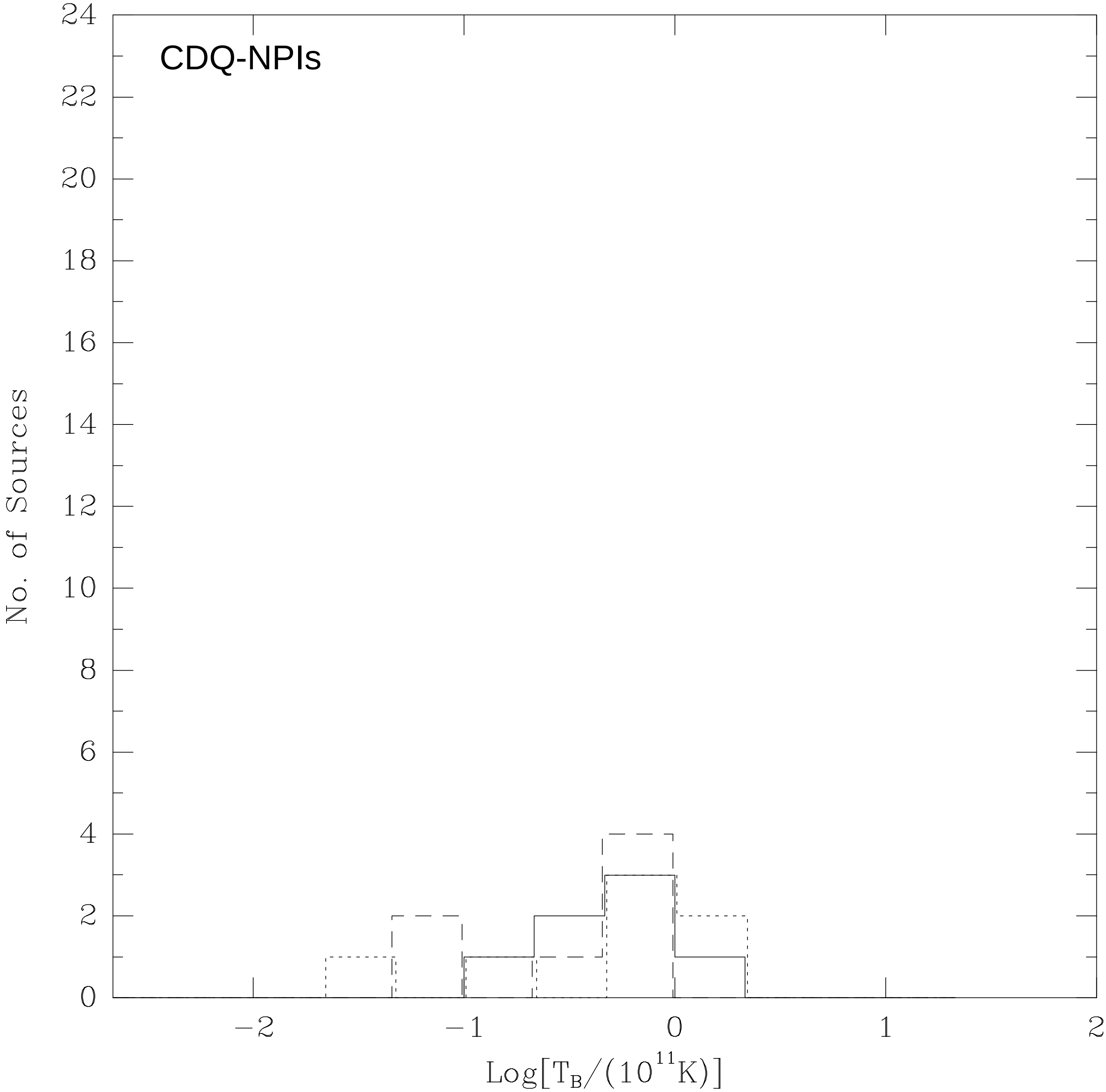
CDQ-NPIs
No. of Sources
Log[T_B/(10^{11}K)]
0
2
4
6
8
10
12
14
16
18
20
22
24
−2
−1
0
1
2

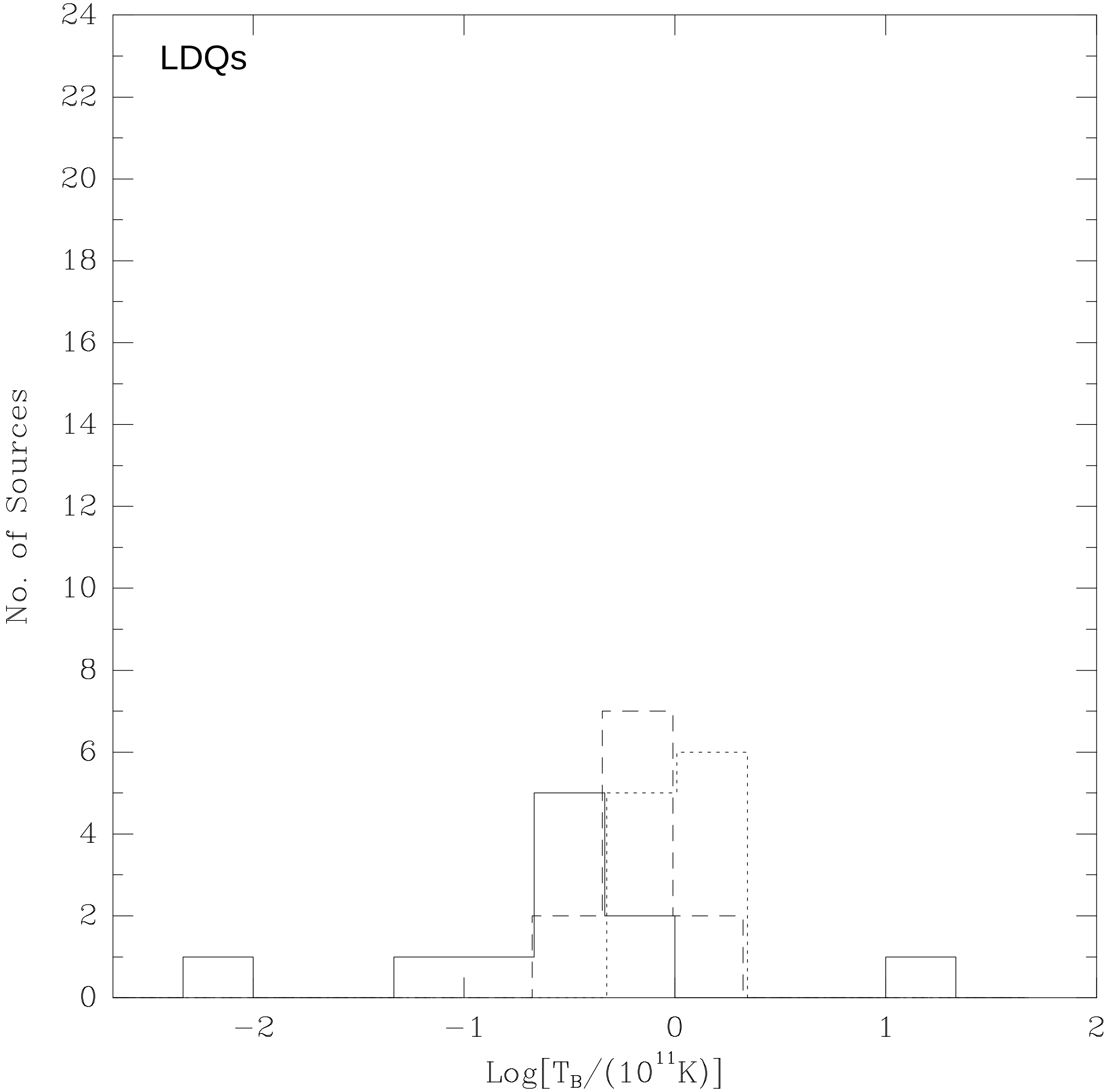
LDQs
No. of Sources
Log[T_B/(10^{11}K)]
0
2
4
6
8
10
12
14
16
18
20
22
24
−2
−1
0
1
2

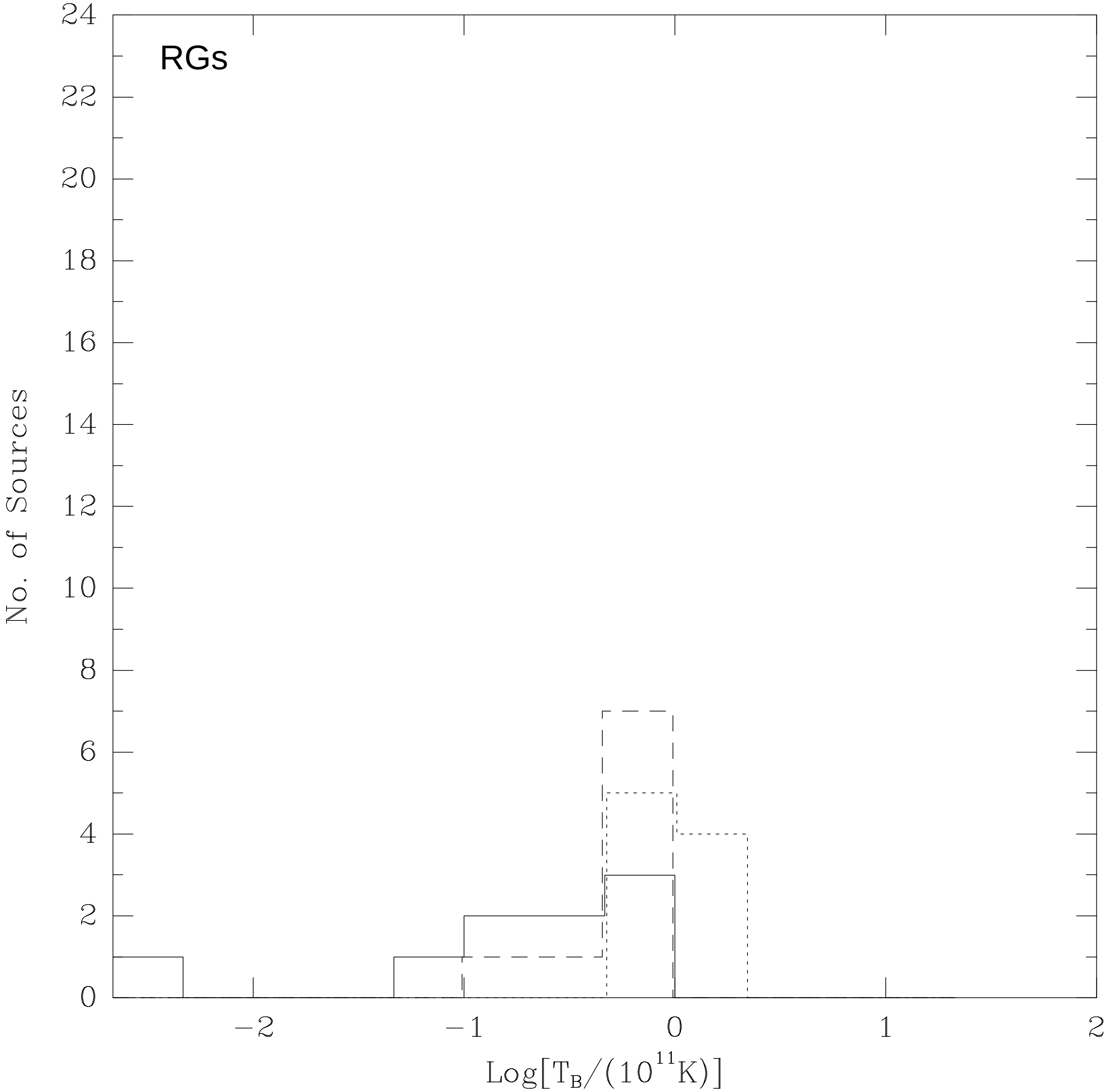
RGs
No. of Sources
Log[T_B/(10^{11}K)]
0
2
4
6
8
10
12
14
16
18
20
22
24
−2
−1
0
1
2

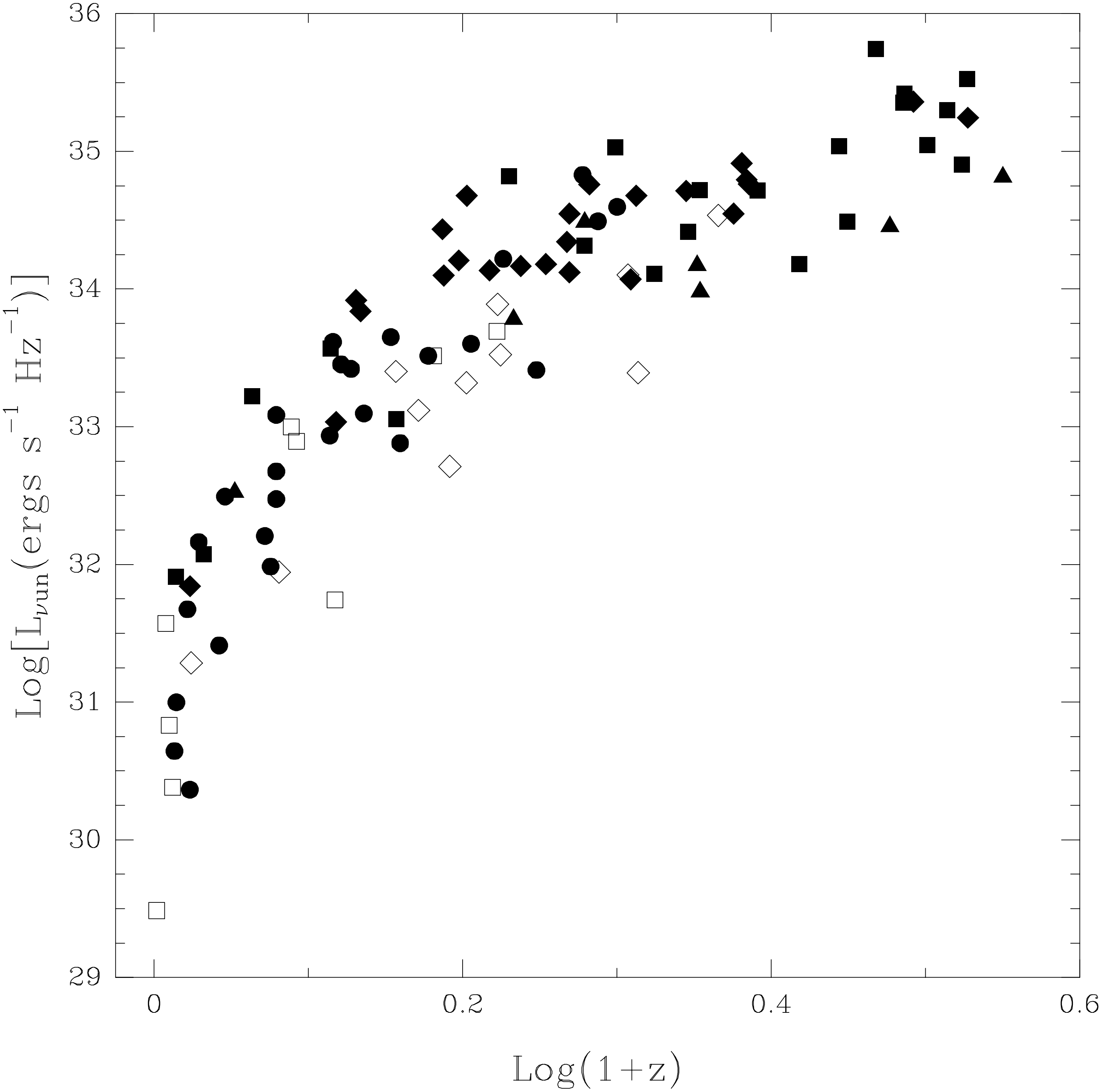

36
35
34
33
32
31
30
29
0
0.2
0.4
0.6
Log[L_νun(ergs s^-1 Hz^-1)]
Log(1+z)

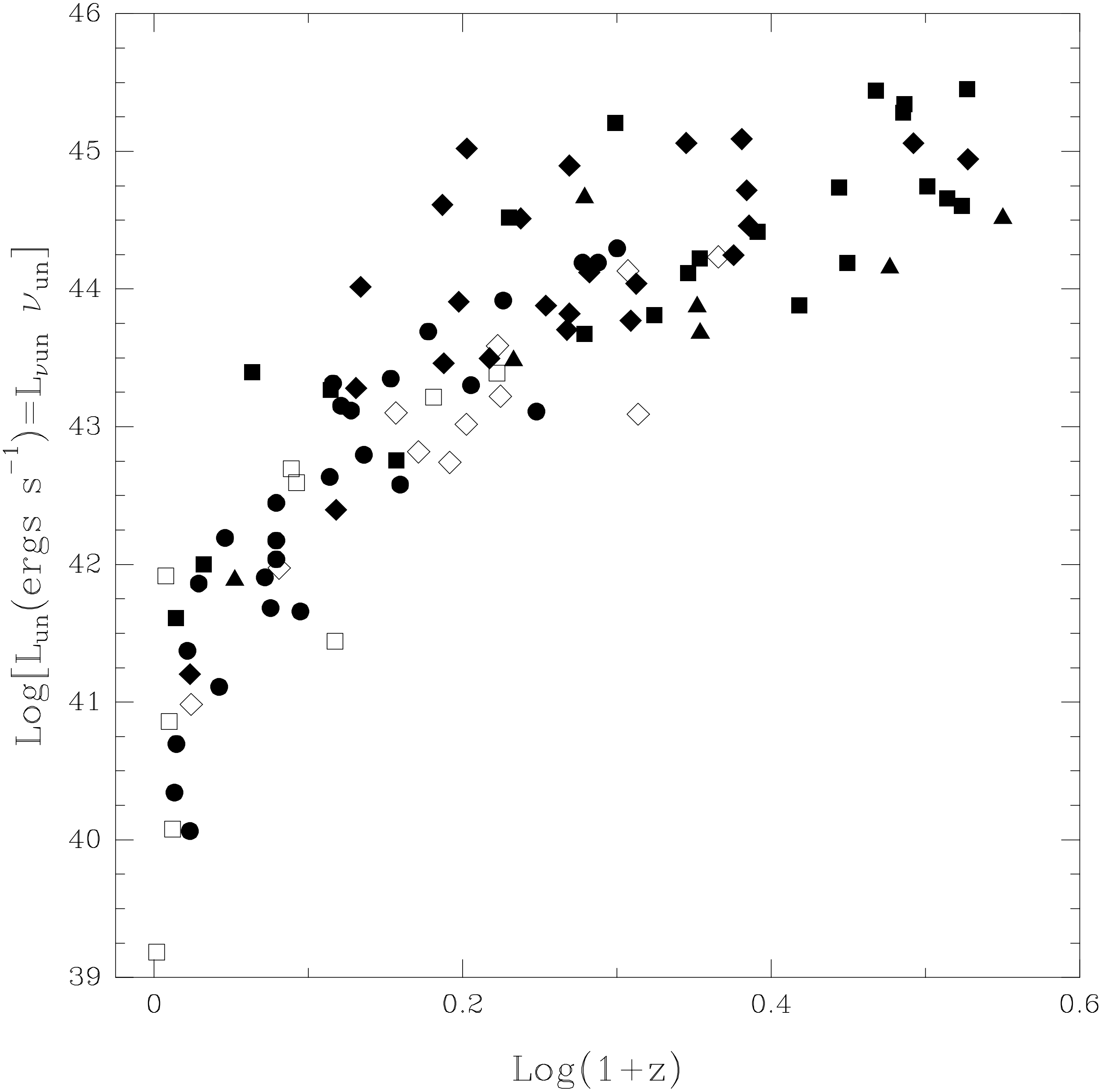

46
45
44
43
42
41
40
39
0
0.2
0.4
0.6
Log[L_{un}(ergs s^{-1})=$L_{\nu un}$ ν_{un}]
Log(1+z)

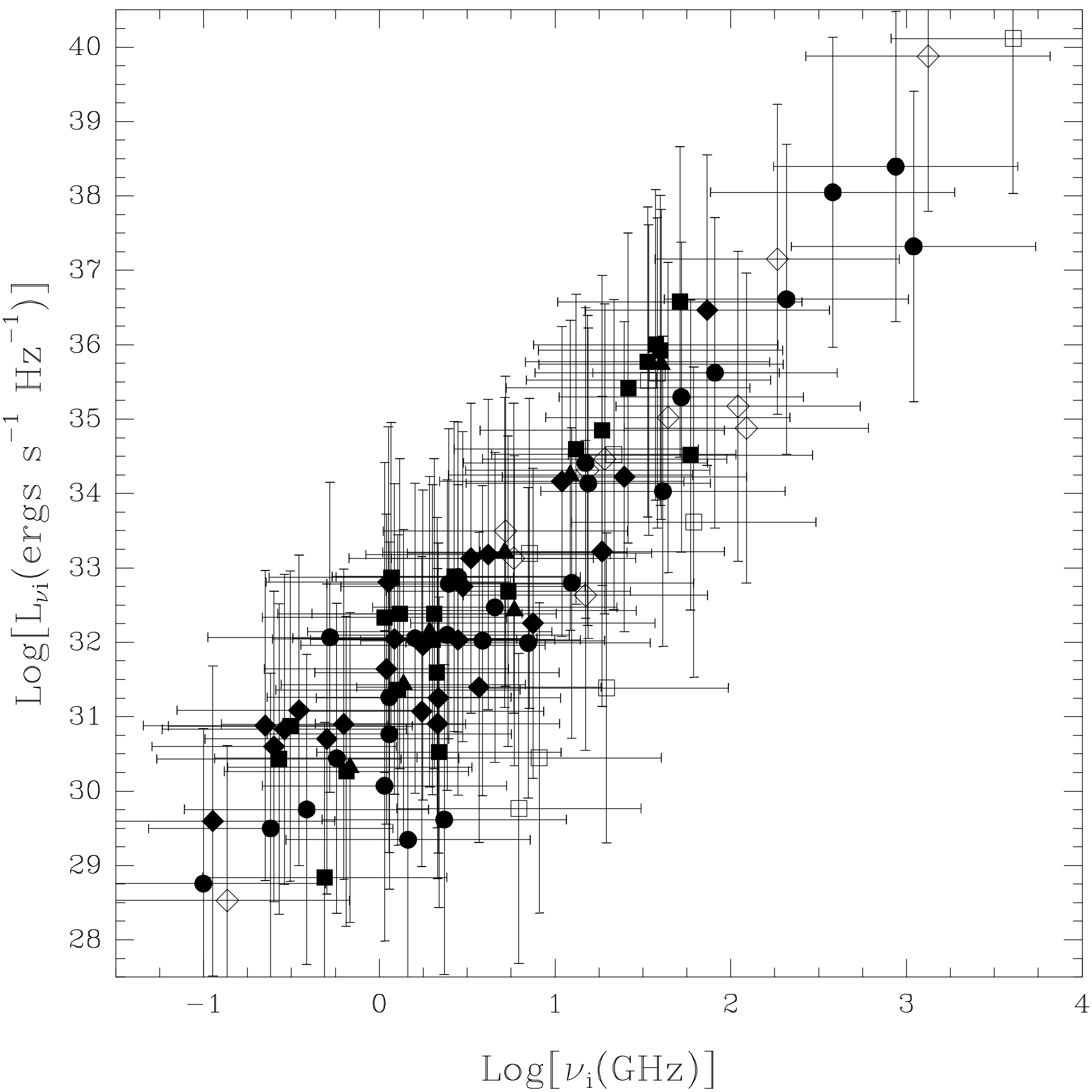

40
39
38
37
36
35
34
33
32
31
30
29
28
$\mathrm{Log}[\mathrm{L}_{\nu\mathrm{i}}(\mathrm{ergs\ s^{-1}\ Hz^{-1}})]$
−1
0
1
2
3
4
$\mathrm{Log}[\nu_\mathrm{i}(\mathrm{GHz})]$

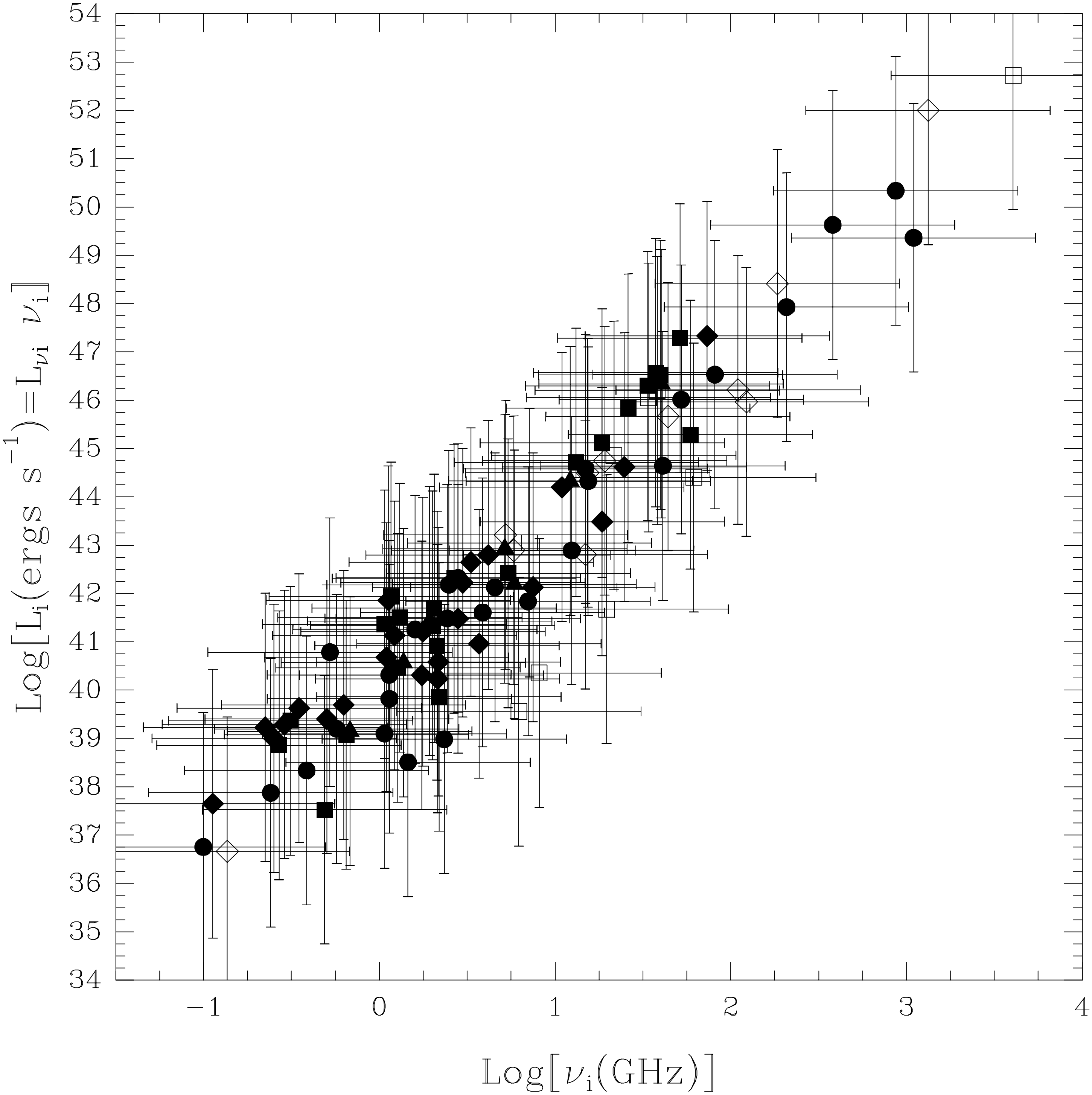

Log[L_i(ergs s^-1)=L_νi ν_i]
Log[ν_i(GHz)]
54
53
52
51
50
49
48
47
46
45
44
43
42
41
40
39
38
37
36
35
34
−1
0
1
2
3
4

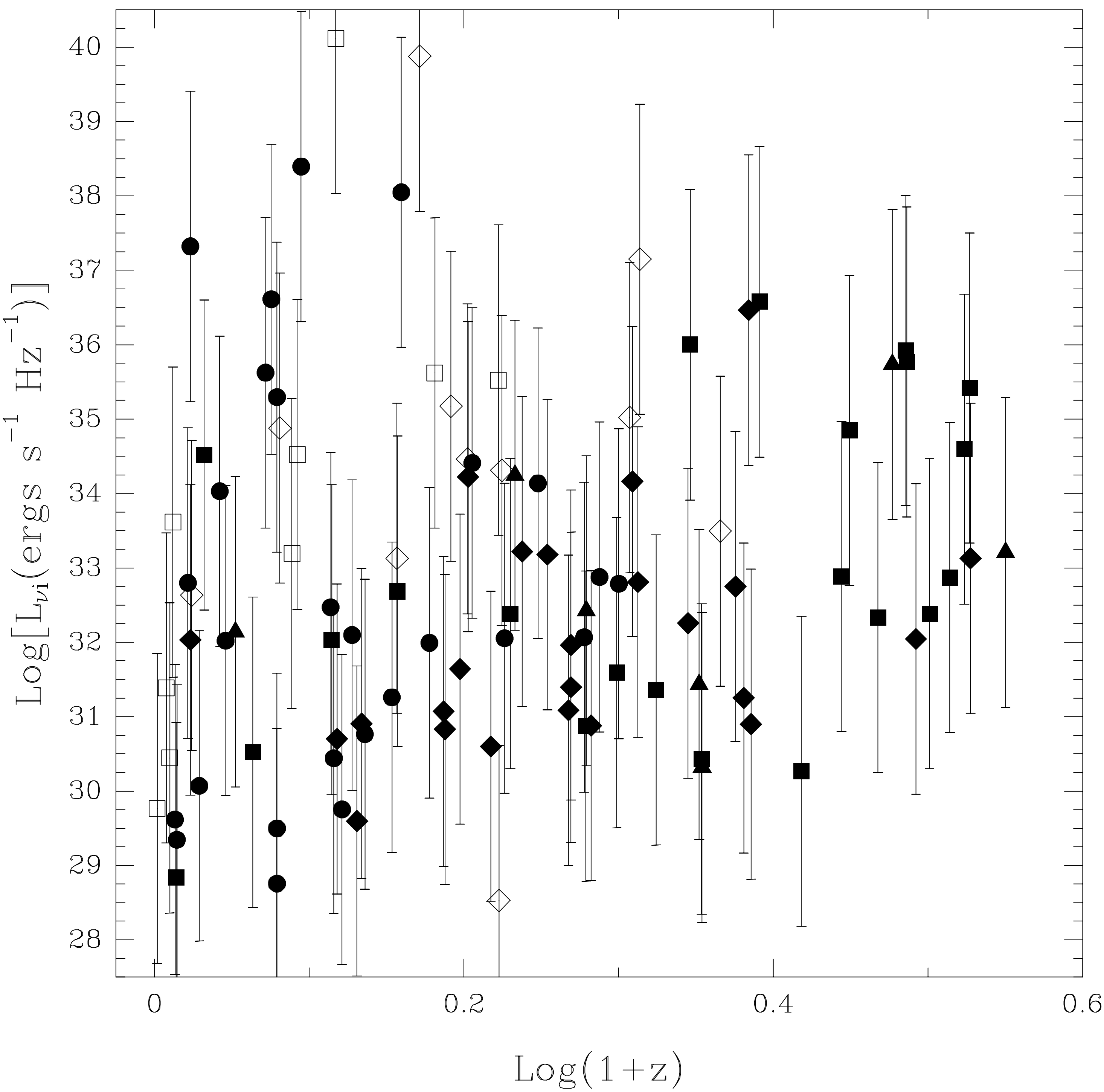

Log[L_νi(ergs s^-1 Hz^-1)]
Log(1+z)
28
29
30
31
32
33
34
35
36
37
38
39
40
0
0.2
0.4
0.6

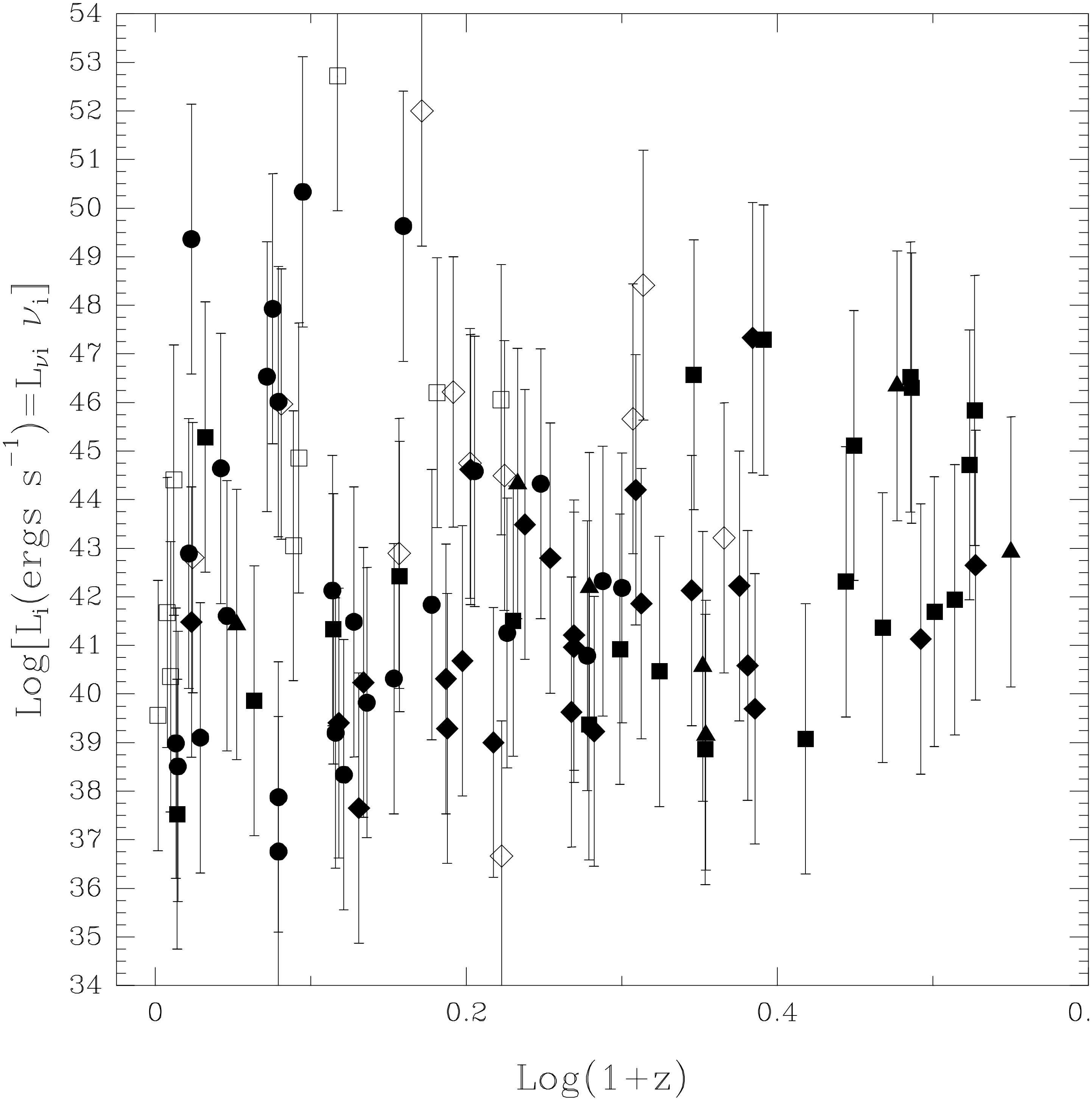

54
53
52
51
50
49
48
47
46
45
44
43
42
41
40
39
38
37
36
35
34
Log[L$_i$(ergs s^{-1})=L$_{\nu i}$ ν_i]
0
0.2
0.4
0.6
Log(1+z)

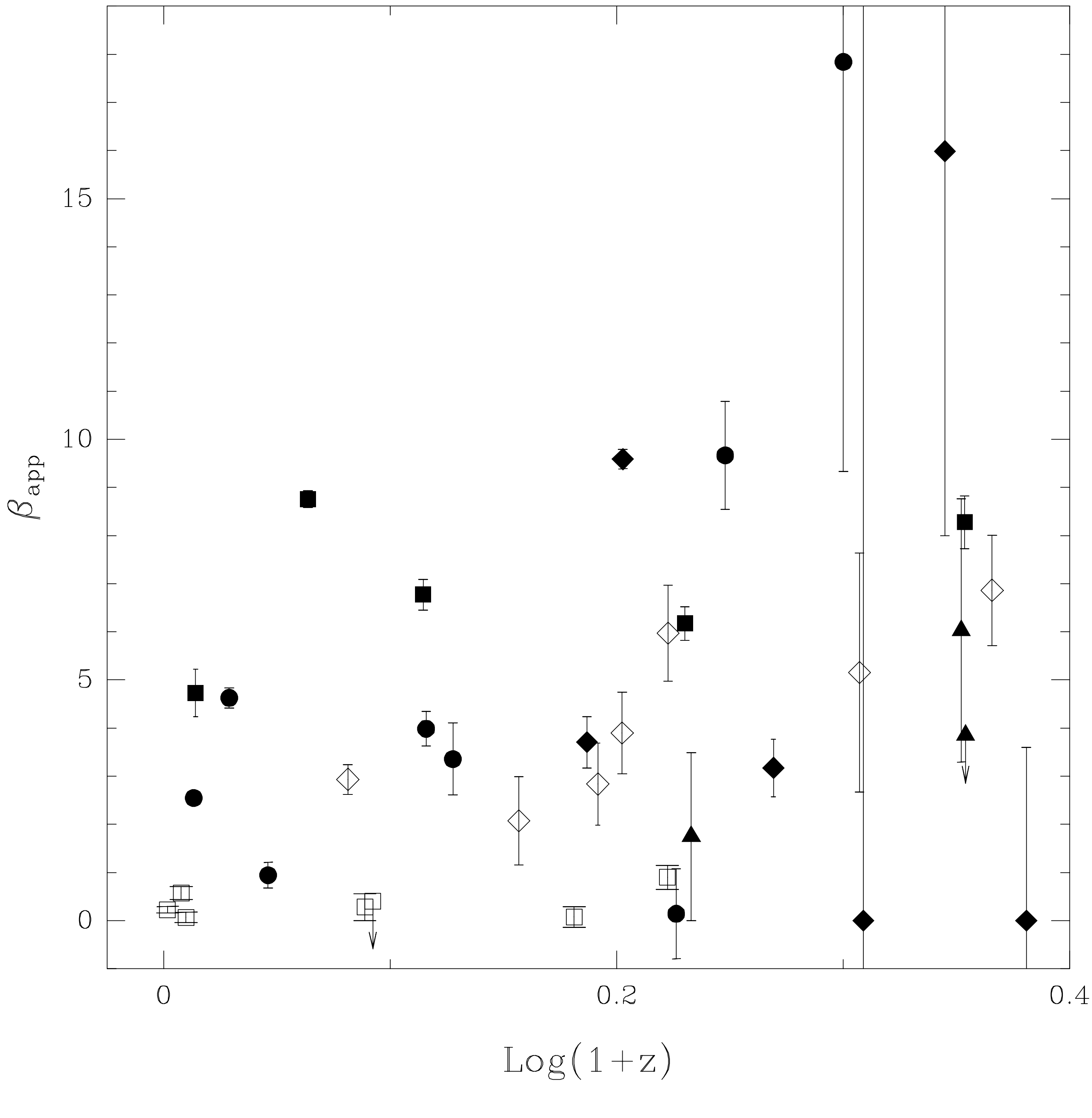

15
10
5
0
0
0.2
0.4
$\beta_{\rm app}$
Log(1+z)

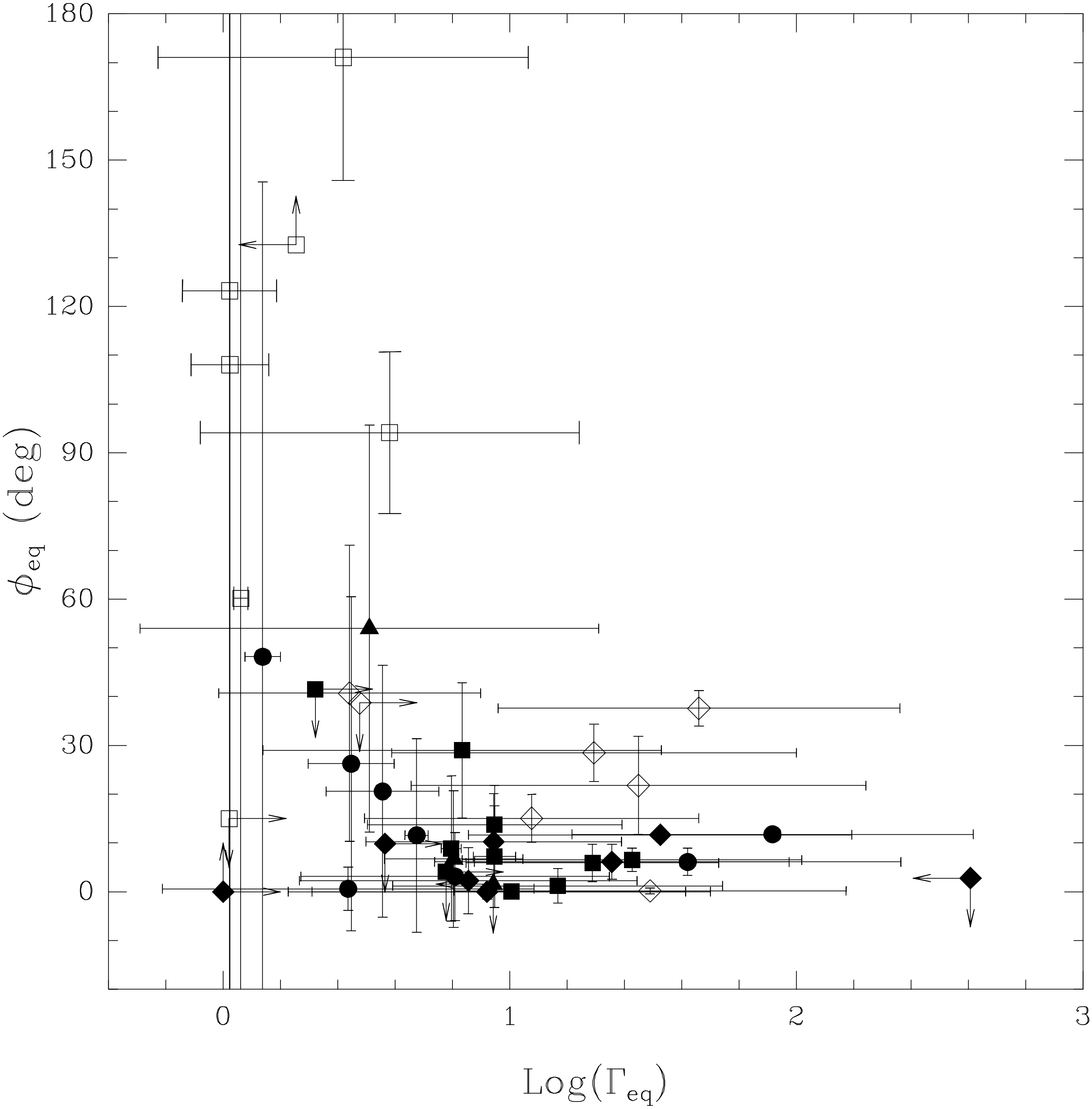

180
150
120
90
60
30
0
ϕ_{eq} (deg)
0
1
2
3
Log(Γ_{eq})

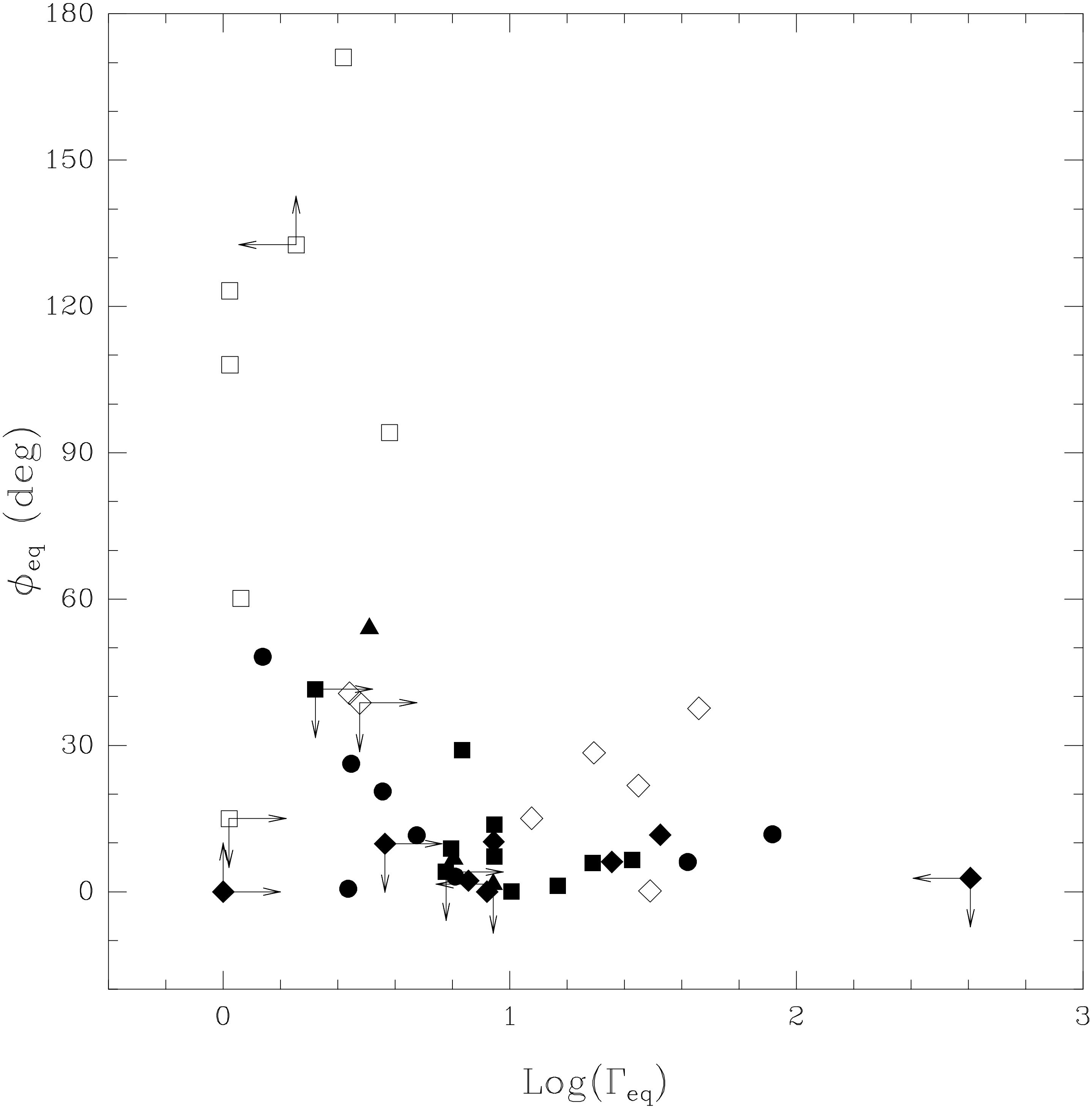

180
150
120
90
60
30
0
ϕ_{eq} (deg)
0
1
2
3
Log(Γ_{eq})

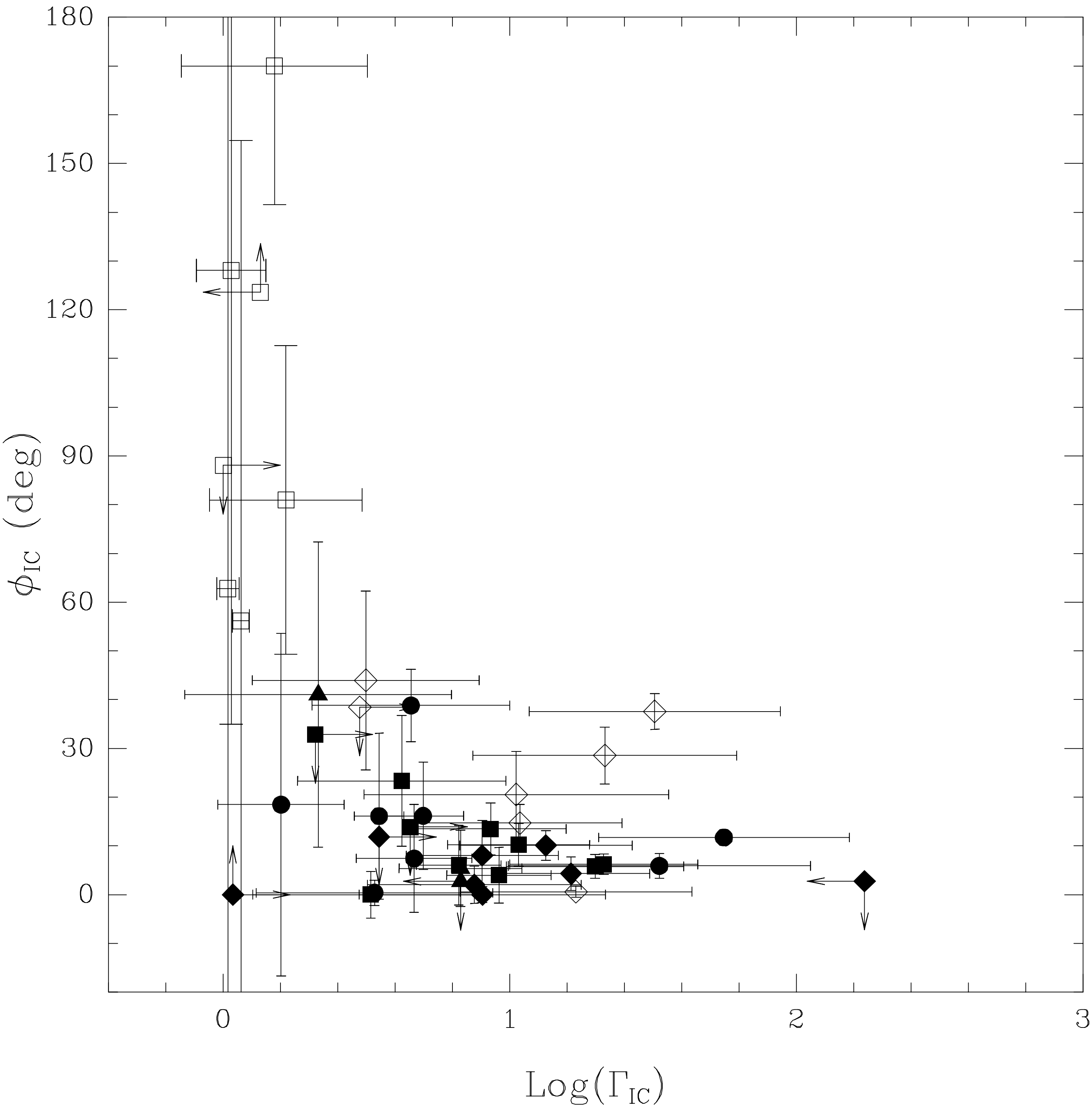
180
150
120
90
60
30
0
ϕ_{IC} (deg)
0
1
2
3
$\mathrm{Log}(\Gamma_{IC})$

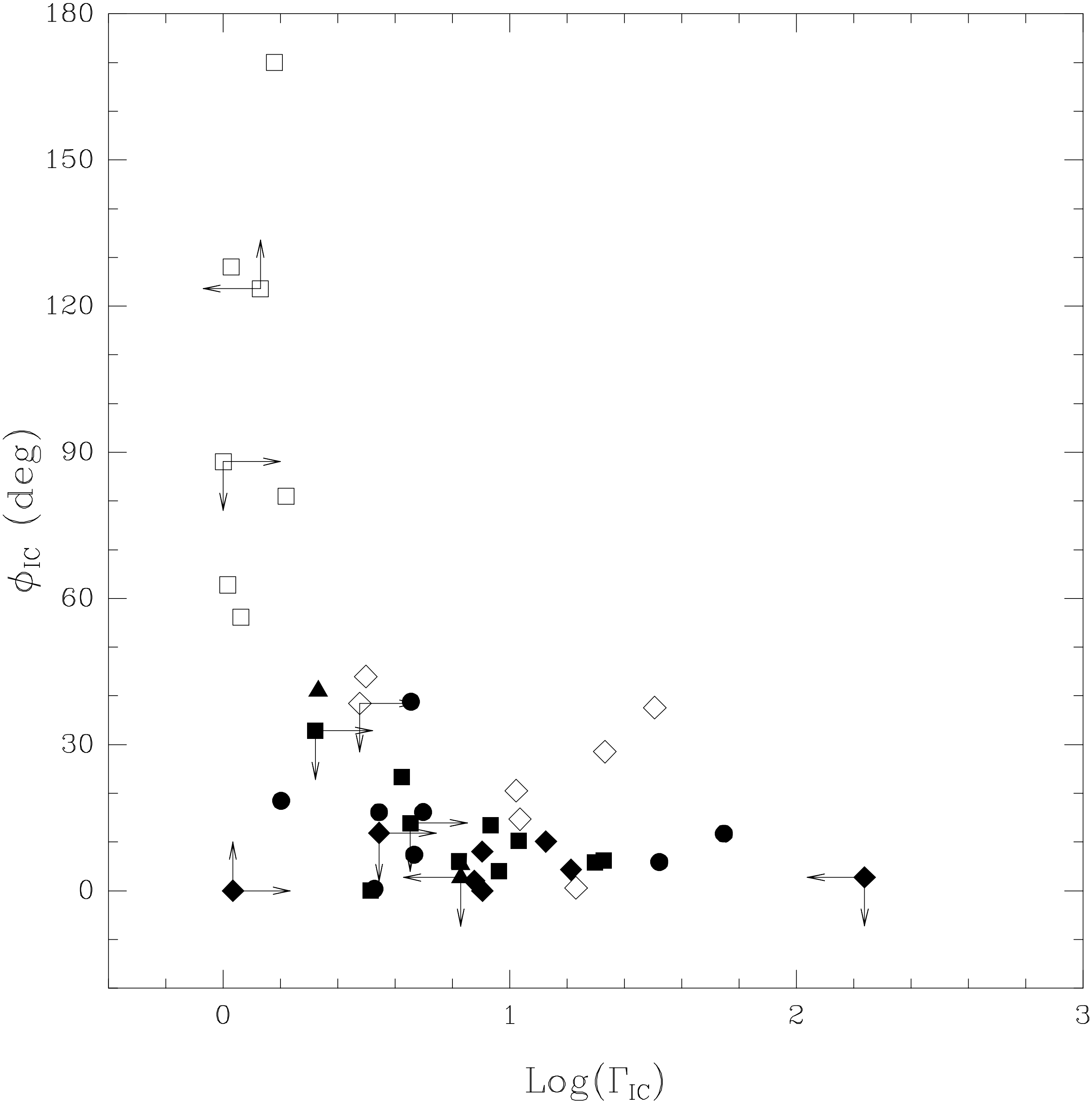

180
150
120
90
60
30
0
ϕ_{IC} (deg)
0
1
2
3
Log(Γ_{IC})

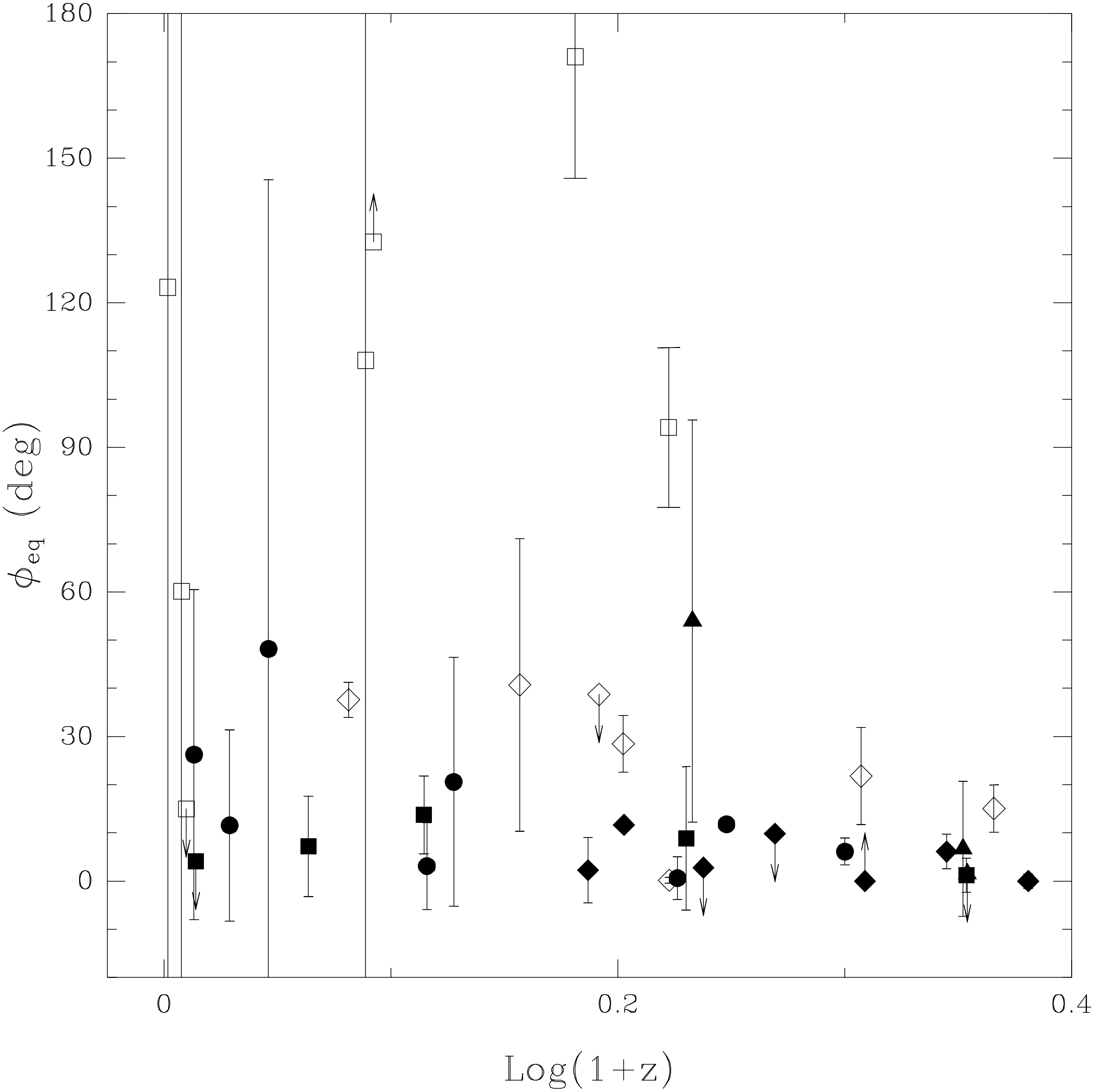

180
150
120
90
60
30
0
ϕ_{eq} (deg)
0
0.2
0.4
Log(1+z)

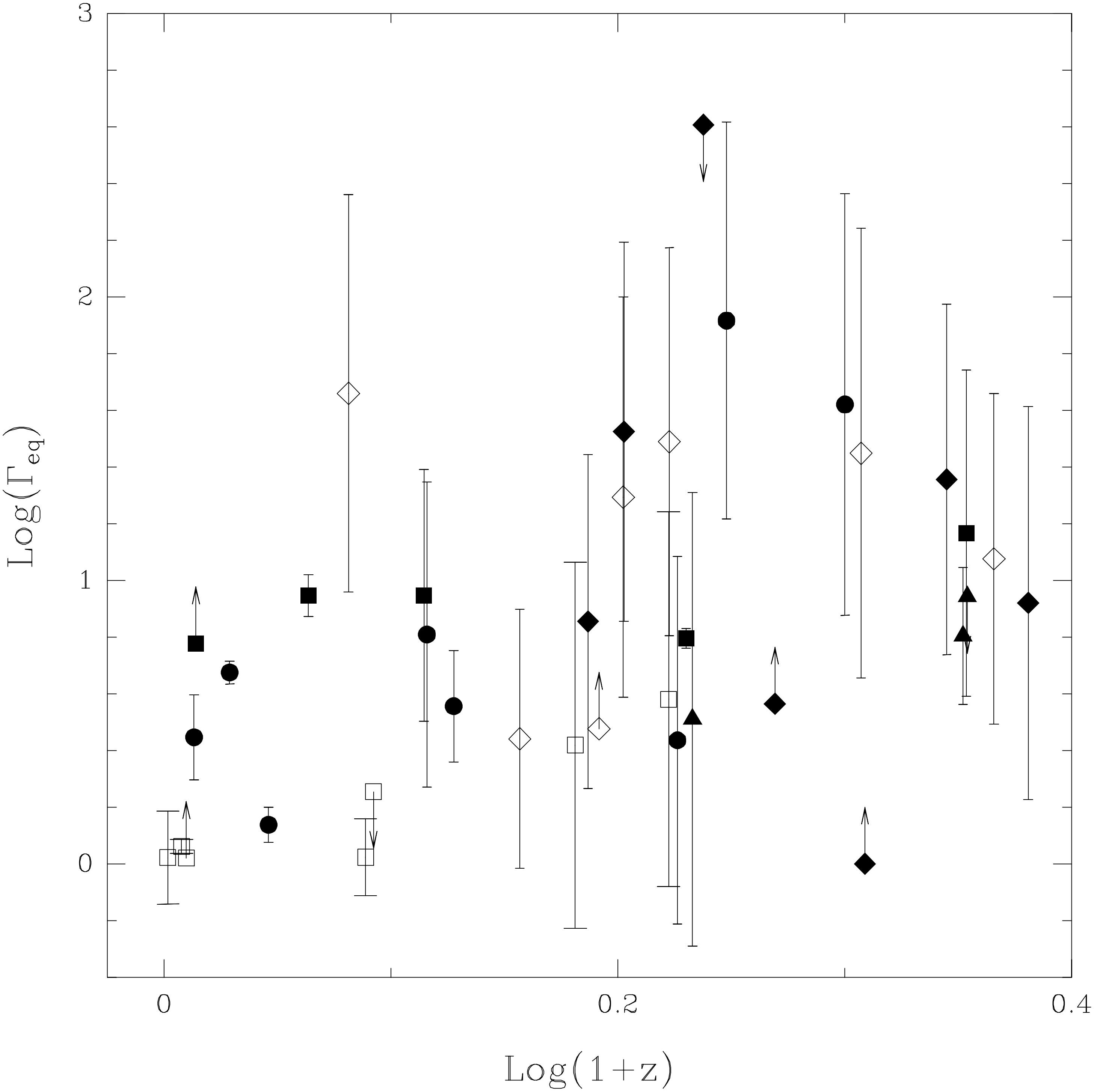
3
2
1
0
Log(Γ_{eq})
0
0.2
0.4
Log(1+z)

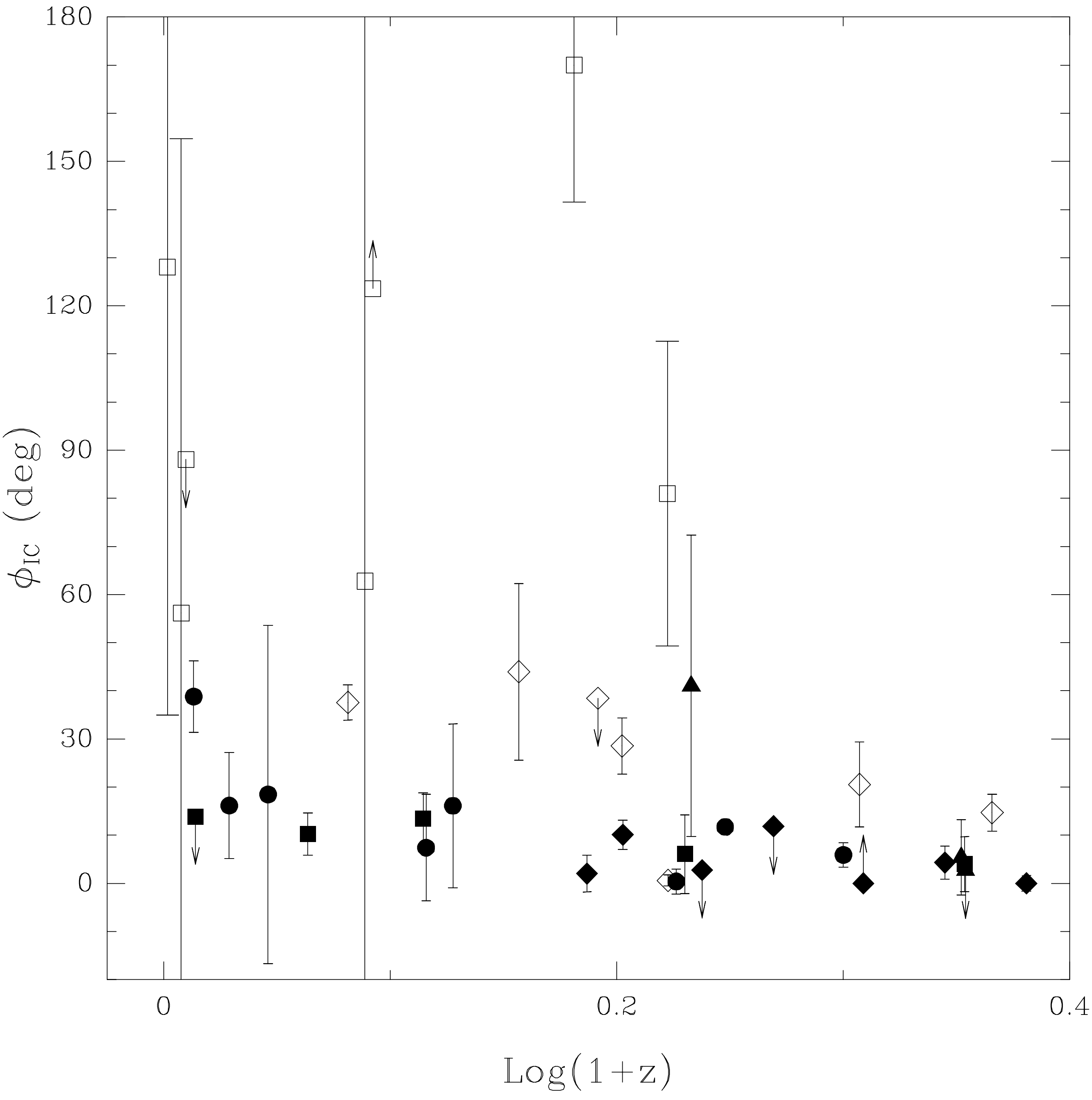

180
150
120
90
60
30
0
ϕ_{IC} (deg)
0
0.2
0.4
Log(1+z)

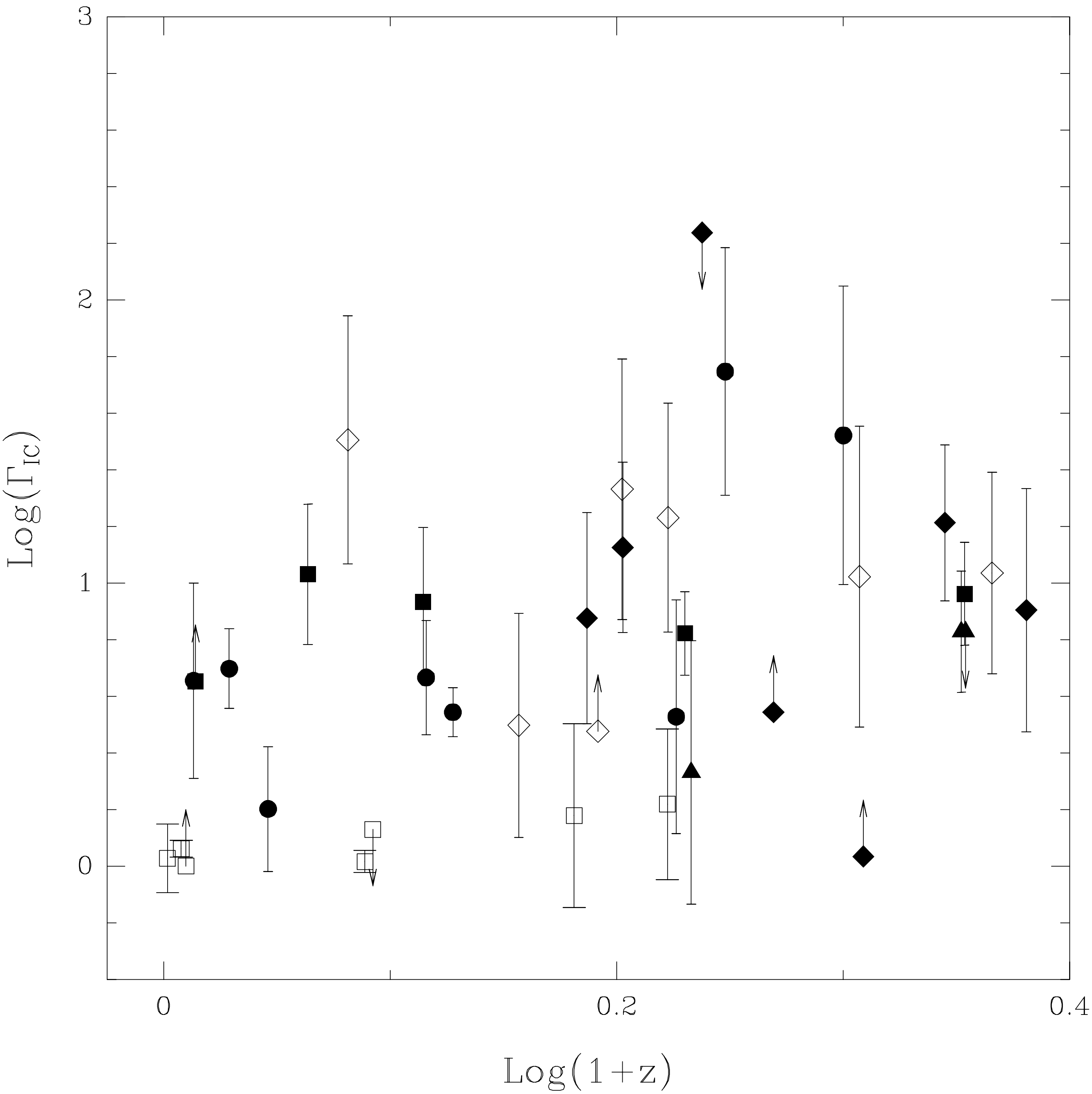

3
2
1
0
Log(Γ_{IC})
0
0.2
0.4
Log(1+z)